

# Dichography: Two-frame Ultrafast Imaging from a Single Diffraction Pattern

Linos Hecht,<sup>1</sup> Andre Al Haddad,<sup>2</sup> Björn Bastian,<sup>3</sup> Thomas M. Baumann,<sup>4</sup> Johan Bielecki,<sup>4</sup> Christoph Bostedt,<sup>2,5</sup> Subhendu De,<sup>6</sup> Alberto De Fanis,<sup>4</sup> Simon Dold,<sup>4</sup> Thomas Fennel,<sup>7</sup> Fanny Goy,<sup>1</sup> Christina Graf,<sup>8,9</sup> Robert Hartmann,<sup>10</sup> Georg Jakobs,<sup>1</sup> Maximilian Joschko,<sup>8,9</sup> Gregor Knopp,<sup>2</sup> Katharina Kolatzki,<sup>1</sup> Sivarama Krishnan,<sup>6</sup> Björn Kruse,<sup>7</sup> Asbjørn Ø. Lægdsmand,<sup>11</sup> Bruno Langbehn,<sup>12</sup> Sudhasattwa Mandal,<sup>5</sup> Tommaso Mazza,<sup>4</sup> Michael Meyer,<sup>4</sup> Christian Peltz,<sup>7</sup> Thomas Pfeifer,<sup>13</sup> Safi Rafie-Zinedine,<sup>4</sup> Antoine Sarracini,<sup>2</sup> Mario Sauppe,<sup>1</sup> Florian Schenk,<sup>14</sup> Kirsten Schnorr,<sup>2</sup> Björn Senftleben,<sup>4</sup> Keshav Sishodia,<sup>6</sup> Frank Stienkemeier,<sup>15</sup> Zhibin Sun,<sup>2</sup> Rico Mayro P. Tanyag,<sup>16</sup> Paul Tümmler,<sup>7</sup> Sergey Usenko,<sup>4</sup> Carl Frederic Ussling,<sup>1</sup> Vanessa Wood,<sup>14</sup> Xinhua Xie,<sup>2</sup> Maksym Yarema,<sup>14</sup> Olesya Yarema,<sup>14</sup> Nuri Yazdani,<sup>14</sup> Hankai Zhang,<sup>2</sup> Bernd von Issendorff,<sup>15</sup> Yevheni Ovcharenko,<sup>4</sup> Marcel Mudrich,<sup>11</sup> Daniela Rupp,<sup>1,\*</sup> and Alessandro Colombo<sup>1,†</sup>

<sup>1</sup>*Laboratory for Solid State Physics, ETH Zurich, 8093 Zürich, Switzerland*

<sup>2</sup>*Paul Scherrer Institut, 5232 Villigen, Switzerland*

<sup>3</sup>*Wilhelm Ostwald Institute for Physical and Theoretical Chemistry, Leipzig University, 04103 Leipzig, Germany*

<sup>4</sup>*European XFEL, 22869 Schenefeld, Germany*

<sup>5</sup>*Laboratory for Ultrafast X-ray Sciences, Institute of Chemical Sciences and Engineering,*

*Ecole Polytechnique Federale de Lausanne (EPFL), 1015 Lausanne, Switzerland*

<sup>6</sup>*Quantum Center of Excellence for Diamond and Emergent Materials and Department of Physics, Indian Institute of Technology Madras, Chennai 600036, India*

<sup>7</sup>*Institute of Physics, University of Rostock, 18051 Rostock, Germany*

<sup>8</sup>*Department of Chemistry and Biotechnology, Darmstadt University of Applied Sciences, 64295 Darmstadt, Germany*

<sup>9</sup>*EUT+ Institute of Nanomaterials & Nanotechnologies EUTINN, European University of Technology, European Union*

<sup>10</sup>*PNSensor GmbH, 81739 Munich, Germany*

<sup>11</sup>*Institute of Physics, University of Kassel, 34132 Kassel, Germany*

<sup>12</sup>*Institute for Optics and Atomic physics, Technical University Berlin, 10623 Berlin, Germany*

<sup>13</sup>*Max-Planck-Institut für Kernphysik, 69117 Heidelberg, Germany*

<sup>14</sup>*Institute for Electronics, ETH Zurich, 8049 Zurich, Switzerland*

<sup>15</sup>*Institute of Physics, University of Freiburg, 79104 Freiburg, Germany*

<sup>16</sup>*Department of Chemistry, Aarhus University, 8000 Aarhus C, Denmark*

X-ray free-electron lasers can nowadays deliver pairs of ultrabright, ultrashort light pulses with controllable delays at different photon energies. When combined with diffraction experiments, the interaction of these pulses with a sample at different times can produce two snapshots of an evolving system, enabling spatial and temporal resolution of ultrafast dynamics in nanomatter at and beyond the terahertz time scale. However, light detectors are orders of magnitude slower. The diffraction signals from the two pulses overlap in the recorded data and cannot be separated using currently available analysis methods. Here, we address this challenge by introducing *Dichography*, a diffraction imaging technique that restores the two unique views of the sample from superimposed scattering signals. We apply *Dichography* to experimental diffraction patterns of isolated xenon-doped superfluid helium nanodroplets, imaged using time-delayed, two-color X-ray pulses at intensities near the detection limit. The reconstructed images provide evidence of the survival of the xenon structures up to 750 fs after the interaction with the first shot. The capabilities of *Dichography* are further explored by applying the method to data from a second experiment, in which we retrieve the images of two distinct silver nanoparticles intercepted by the same light pulse. *Dichography* enables a new class of experiments for spatially and temporally resolving ultrafast phenomena, making a significant step toward the original promise of X-ray free-electron lasers to capture ultrafast movies of nanomatter.

## I. INTRODUCTION

Diffraction experiments are a central method to study ultrafast structural changes in matter when combined with the ultra-short and ultra-bright coherent light pulses delivered by extreme ultraviolet and X-ray Free Electron Lasers (XFELs). XFELs can nowadays deliver individual pulses with a duration of a few tens of femtoseconds down

to hundreds of attoseconds [1–5]. The light diffracted from the sample, recorded by a suitable detector, provides a high-resolution structural fingerprint of the system under study, with a time resolution equivalent to the duration of the light pulse.

Among diffraction-based techniques, single-particle Coherent Diffraction Imaging (CDI) stands out for its capability to retrieve the full electronic density of isolated nanostructures from a single diffraction image produced by an individual light pulse [6, 7]. Thus, since the pioneering era of XFELs [8], CDI has been an invaluable tool for capturing ultrafast snapshots of fragile nanoscale ob-

\* rupppda@phys.ethz.ch

† alcolombo@phys.ethz.ch

jects in free-flight [9–13] and their light-driven dynamics [14–18].

Dynamical investigations are mostly performed with *pump-probe* schemes: processes in the system are triggered by a first laser pulse – the *pump* – and its structural and electronic properties are probed by an XFEL flash that interacted with the sample at a specific time delay – the *probe*. Often, the *pump* laser covers spectral regions from the near infrared to the ultraviolet. At the corresponding photon energies of a few eV, only a subset of the possible light-induced ultrafast processes can be triggered and, thus, investigated. Furthermore, the *pump* doesn't provide any structural information on the sample, whose features are at the nanometer length-scale – well beyond the resolution limit of the UV or longer-wavelength laser radiation.

Thanks to recent technical developments, XFELs can deliver pairs of light pulses in the XUV or X-ray spectrum [1, 19–24]. Both pulses retain the coherence, brightness, and ultrashort nature of conventional XFEL pulses; their wavelength can be independently tuned, and their arrival time at the interaction region can be controlled with high precision. This novel capability, known as *two-color* mode, unlocks a whole new class of dynamical investigations, where the XFEL delivers both the *pump* pulse, which triggers the dynamics in a pristine sample, and the *probe* pulse, which probes the evolved state. When the *two-color* capability of XFELs is combined with the high spatial resolution of diffraction imaging, the sample's structure can be accessed at two different points in time. The femtosecond precision at which the time delay between the two light pulses can be controlled paves the way for two-frame movies of structural dynamics reaching the terahertz realm, and potentially well beyond.

However, light detectors are several orders of magnitude slower [25–27]. They cannot be triggered or read-out quickly enough to individually capture the diffraction of the *pump* and the *probe* shots. As a consequence, the sum of their signal is recorded in a single diffraction image. Conventional algorithmic methods for CDI, necessary to restore the sample's image from the acquired scattering data [6, 7, 28] are not applicable.

Significant effort had been devoted to overcoming this technical limitation by physically separating the two scattering images. First successful realizations achieved this by placing spectral filters [29, 30] or by directing the pulses onto two different detectors via optical devices [31]. Nevertheless, these solutions come with significant trade-offs, e.g., strongly reduced signal brightness, restricted range of viable photon energies, reduced control on the time delay, or partial loss of scattering information. Therefore, developing new methods to fully exploit *two-color* pulses across various diffraction-based experimental approaches remains a top priority for the scientific community.

In this work, we introduce *Dichography* (from *dichos*, meaning “in two”), an imaging method that enables the reconstruction of two sample images from superimposed

diffraction signals. *Dichography*, applicable under a variety of experimental conditions, unlocks the full imaging potential of *two-color* diffraction patterns by disentangling the scattering contributions in the recorded data, to reconstruct the two, distinct, *views* of the sample as “seen” by the individual pulses.

We perform *dichographic* imaging for two different experimental conditions. In one case, a pair of light pulses of different wavelengths delivered by the European XFEL intercepts superfluid helium nanodroplets doped with xenon. Despite the low photon yield in the diffraction signal – for such a highly photon-demanding approach – successful reconstructions can be achieved for a subset of optimal diffraction patterns. The retrieved *frames* are two snapshots of the same xenon-doped helium droplet, delayed in time by 750 fs. Similar structures can be identified in the two frames, indicating that extended damages to the sample due to the interaction with the first XFEL pulse only happen at longer time scales.

In a second experimental case, pairs of silver nanoparticles are simultaneously present in the focus when single light pulses delivered by the SwissFEL reach the interaction region. When the two samples have enough spatial separation, the interference of their scattered fields is not resolved by the detector. In this case, the properties of the imaging problem, i.e. the mathematical connection between the sample and the acquired data, become analogous to the *two-color* situation. Therefore, *Dichography* can be employed to restore the images of the two particles, demonstrating its flexibility and performance under different conditions.

The imaging quality achieved by *Dichography* is strictly connected to the present understanding of the underlying mathematical and numerical challenges, as well as to the current performance of XFELs. With this work, we aim at stimulating and encouraging research efforts in both directions. In this regard, the possible applications of *Dichography* with the currently available experimental possibilities are discussed, along with concepts that could be viable in the near future.

The demonstration of *Dichography*, and its possible improvements and extensions to closely related imaging challenges, unlock novel and exciting possibilities for the study of ultrafast structural dynamics resolved in both time and space.

## II. THE DICOGRAPHIC PROBLEM

*Dichography*, similar to conventional CDI, is an *indirect* imaging method. The sample image is retrieved from the acquired diffraction data via algorithmic methods, designed to solve the specific *imaging problem*.

In conventional CDI, the image recorded by the detector,  $I(\vec{q})$ , is the square amplitude of the scattered field  $\psi(\vec{q})$ . The field carries the full information on the sample density  $\rho(\vec{x})$ . However, only its magnitude  $|\psi(\vec{q})| = \sqrt{I(\vec{q})}$  is experimentally accessible, while the

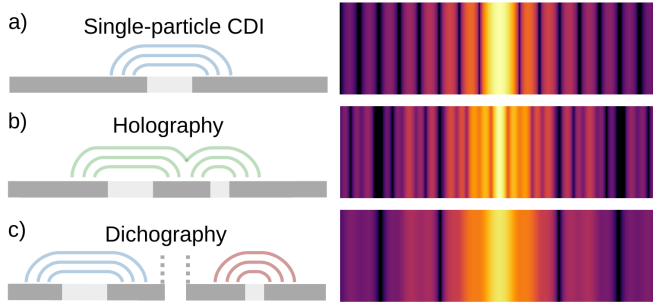


FIG. 1. Intuitive representation of the difference between conventional single-particle CDI, *Holography*, and *Dichography* in terms of a double-slit experiment. In a), the incoming radiation intercepts a single slit, and the recorded scattering image encodes its size. In b), the fields scattered by two apertures interfere with each other. The *far-field* intensities thus encode the information on the size of both slits and their relative distance. In c), the fields produced by the two apertures do not interfere. The diffraction signal, thus, only encodes the independent properties of the two slits.

field's phase is lost. Therefore, it is necessary to retrieve the phase to obtain the sample image  $\rho(\vec{x})$ . In CDI, the *phase retrieval problem* is numerically solved by specifically designed *phase retrieval algorithms* [7, 32].

The imaging problem in *Dichography* is significantly more demanding. Indeed, *Dichography* deals with situations where the acquired scattering data  $I(\vec{q})$  is the incoherent sum of the intensities of two independent scattered fields  $\psi^A(\vec{q})$  and  $\psi^B(\vec{q})$ , that is:

$$I(\vec{q}) = I^A(\vec{q}) + I^B(\vec{q}) = |\psi^A(\vec{q})|^2 + |\psi^B(\vec{q})|^2. \quad (1)$$

The two fields encode two different electronic densities  $\rho^A$  and  $\rho^B$ , which correspond to the two independent images of a sample. Thus, the *dichographic* imaging problem consists in retrieving the phase of  $\psi^A(\vec{q})$  and  $\psi^B(\vec{q})$ , as well as their relative amplitude contribution to the recorded signal  $I(\vec{q})$ .

Fig. 1 provides an intuitive comparison between the use case of *Dichography* and those of single-particle CDI and *Holography*, using a double-slit diffraction experiment as a reference. As previously mentioned, conventional CDI, illustrated in Fig. 1a, addresses the reconstruction of a single isolated sample, denoted by  $\rho$ . In contrast, *Holography*, depicted in Fig. 1b, involves two distinct samples,  $\rho^A$  and  $\rho^B$ . This configuration necessitates the interference of the two resulting scattering fields at the detector, which fundamentally differs from the *Dichography* approach shown in Fig. 1c.

While *Dichography* is designed to deal with *two-color* diffraction images, its applicability further extends to diverse experimental schemes where the link between the recorded data and the samples under study follows Eq. (1). For this reason, we can generically address  $\rho^A$  and  $\rho^B$  as the two *frames* of a *dichographic* reconstruction. The two *frames* are, conceptually, independent from each other and can be structurally unrelated.

The imaging algorithm at the core of *Dichography*, which disentangles the scattering contributions and retrieves the two frames, is a fundamental result of this work. Its structure is derived from that of conventional *iterative phase retrieval algorithms* for single-particle CDI, adapted to accommodate the specific characteristics of *Dichography*. In fact, it comprises of two iterative phase retrieval processes, each retrieving a frame. The two processes are solely entangled when the experimental diffraction data is constrained: the two estimated intensities are rescaled such that their sum corresponds to the recorded scattering image. A detailed description of the algorithm's workflow and its connection to the CDI counterpart is deferred to Appendix A. We now turn to an investigation of the performance of *Dichography* in two different experimental situations.

### III. RESULTS

#### A. Seeing double from a single shot

The first set of results concerns the analysis of diffraction patterns produced by two particles struck by the same XFEL shot, known as “double-hits”. Although they are of lower scientific relevance compared to two-color diffraction images, they serve as a valuable probe for investigating the capabilities, performance, and key features of *Dichography*.

Here, pairs of silver nanoparticles, simultaneously present in the XFEL focus, are intercepted by a single light pulse delivered by SwissFEL [33]. When the particles are far enough apart, the interference term between the two scattered fields is not resolved by the detector. The recorded diffraction image is, in practice, the incoherent sum of the two intensities, suitable for imaging with *Dichography*. The two retrieved *frames* correspond to the electron density of the two different particles. Further experimental information are provided in Appendix D 1.

The first *dichographic* imaging is shown in Fig. 2. The images of the two particles in Fig. 2b and 2c are the two frames retrieved from the experimental diffraction pattern reported in Fig. 2a, without prior information regarding the particles' shape, size, or orientation. The reconstructions reveal that the experimental image is produced by two silver nanocubes of slightly different sizes and alignment. Due to the cubic structure of the two samples and their orientation, each cube produces strong streaks with four-fold symmetry in the diffraction image. A total of eight streaks can be indeed identified in the diffraction pattern in Fig. 2a.

It is possible to disentangle the two contributions to the scattering, i.e. to calculate the corresponding single-particle diffraction images from the two reconstructed frames. Fig. 2d and Fig. 2e report the two disentangled scattering contributions from the first (Fig. 2b) and second (Fig. 2c) frames, respectively. There, we can ap-

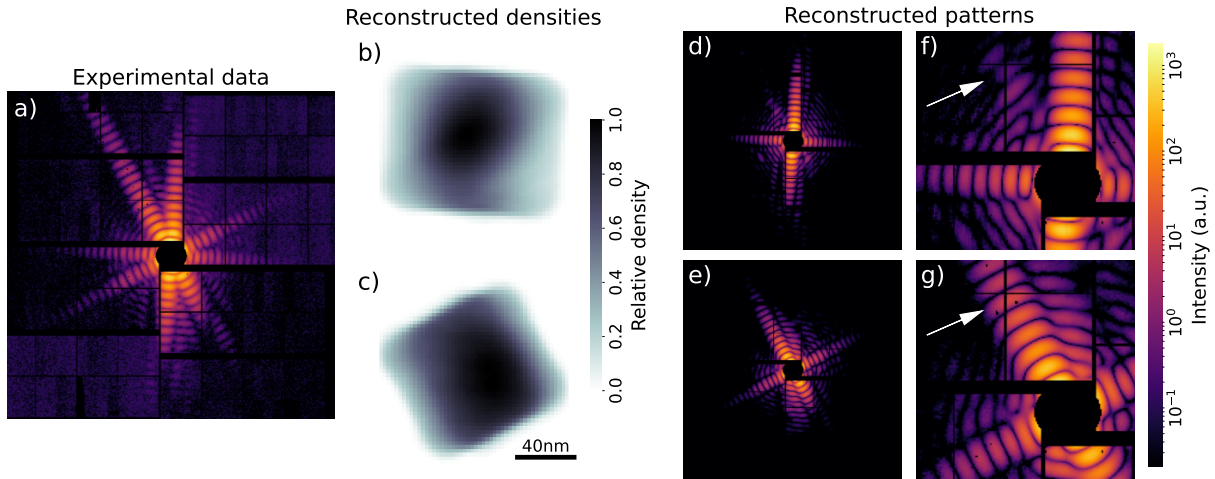


FIG. 2. Example of *dichographic* reconstruction from a single diffraction pattern produced by a “double-hit”. The experimental diffraction data from an individual light pulse delivered by SwissFEL is shown in a). The two particles density retrieved from a) via *Dichography* are shown in b) and c). The two reconstructions correspond to two silver nanocubes, with edge length of around 100 nm. Once the two particles have been reconstructed, the corresponding single-particle diffraction patterns can be calculated, shown in d) for the reconstruction in b), and in e) for the one reported in c). The central parts of the disentangled diffraction images in d) and e) are magnified in f) and g), respectively. The white arrows point at the same region of the diffraction data in a), d), e), f) and g). All diffraction data in a), d), e), f) and g) are plotted with logarithmic color scale.

preciate the capability of *Dichography* to separate the two contributions to the scattering superimposed in 2a, by reproducing the four-fold symmetry of the two cubes with different orientations. This is further enhanced by a closer view in the central part of the separated patterns where the strongest contribution to the scattering signal is concentrated, provided in Fig. 2f and 2g.

From these zoomed-in representations of the disentangled scattering signals, it is also possible to identify few regions where the intensities are not fully disentangled. For example, the white arrows in Fig. 2f and Fig. 2g indicate the same coordinates in the two patterns. In Fig. 2g, this area correspond to a high intensity streak in the direction of cube facets, as visible from the reconstruction in Fig. 2c. Despite the absence of any related structural feature in the other reconstructed frame in Fig. 2b, its disentangled pattern in Fig. 2f still presents traces of this strong scattering signal. This signal marginally affects the inner density profile in Fig. 2c, slightly distorted in the direction of the cube facets of the other frame. We refer to this “cross-talking” between the two frames – where features in one create slight artifacts in the other due to strongly differing scattering intensity in specific directions – as *ghosting*. On the other hand, the intensities mistakenly assigned to the first frame in Fig. 2f are about two orders of magnitude lower than those correctly retrieved in Fig. 2g. This is evident from the logarithmic color map on the right and underscores the ability of *Dichography* to separate the two signals, even when their intensities differ strongly.

Further reconstruction attempts on diffraction patterns extracted from the same dataset of Fig. 2 are presented in Fig. 3. These examples are selected to highlight

how *Dichography* performs on different sample configurations. For instance, Fig. 3a shows a reconstruction which reveals a pair of nanostructures with completely different geometries, a cube and a triangle, strongly underlining how this method neither requires any specific constraint in terms of sample’s structure, nor structural links between the two frames. The reconstruction in Fig. 3b has an additional challenging aspect. Here, the spatial extension of the two samples differs significantly, with the smaller one being around 100 nm in maximum size and the second reaching around 200 nm. As a consequence, the smaller sample could “fit” into the larger one, potentially rendering the separation of the two frames of the reconstruction a significantly harder task. In both Fig. 3a and Fig. 3b, *ghosting* artifacts are barely visible in the form of line-shaped density fluctuations aligned with the hard edges of the reconstruction in the other frame.

Another particular case is shown in Fig. 3c. Here, one sample has a highly symmetric hexagonal morphology, while the other reconstructed density is an agglomerate of two cubes. The apparent empty space between the two cubes, visible due to the accidental perfect alignment of their faces with the FEL pulse, is actually caused by the residual material that coats the nanoparticles in the buffer solution. This buffer is crucial for maintaining stable aerosol injections and ensuring the colloidal stability of the nanoparticles. Thanks to a scattering cross-section significantly lower than silver, it appears mostly transparent in CDI reconstructions. Despite being two separated particles, the two nanocubes are reconstructed together in the same frame with their relative placement, as their interference signal is resolved by the detector. The spatial separation of the hexagonal particle from the

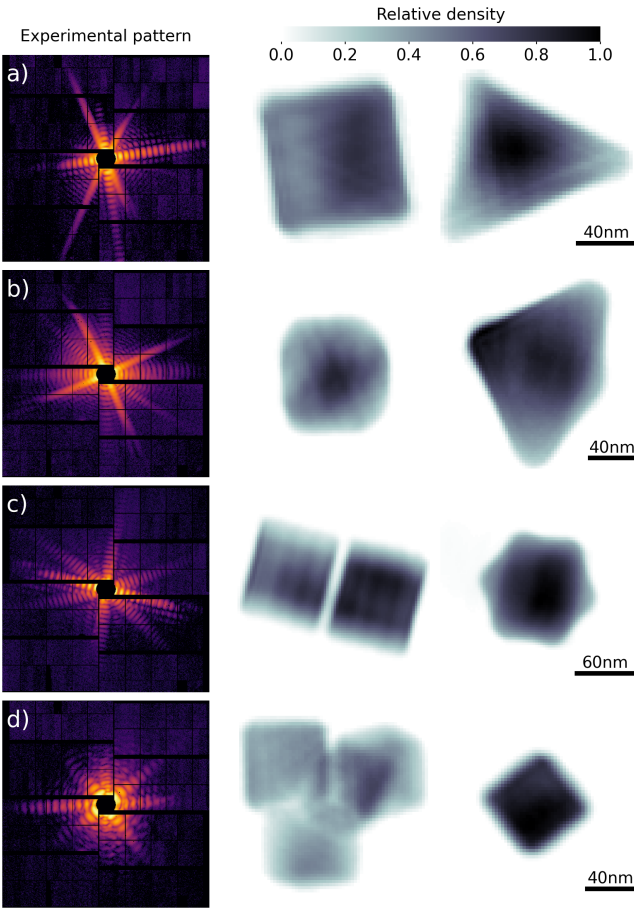


FIG. 3. Further *Dichography* reconstructions of silver nanoparticles from individual diffraction patterns acquired at SwissFEL. Each sub-figure, from a) to d), reports different imaging results on a single diffraction pattern. The experimental data are shown in the leftmost column. The central and rightmost columns report the two frames of the reconstruction. Similar to Fig. 2, within the same sub-figure the two reconstructed densities are reported with common color scale and scale bar, such that their size and brightness can be compared.

cube pairs is, instead, large enough to render the interference term undetected. Therefore, it is reconstructed by *Dichography* in a separate frame.

The last example on “double-hit” data is reported in Fig. 3d, and presents many peculiarities of the samples shown before in one. The two frames of the reconstruction have a significantly different spatial extension, 80 nm for the smaller and up to a maximum of 200 nm for the larger. The smaller density has a simple cubic architecture, whereas the larger one can be interpreted as an agglomerate of four nanocubes. The shape of three cubes in the agglomerate is well imprinted into the overall outline, while the presence of the fourth cube is only revealed thanks to the successful reconstruction of the density values inside the sample. Furthermore, the inner fourth cube in the agglomerate doesn’t come from a

*ghosting* artifact of the cube in the other frame: their orientation is, indeed, slightly different.

The results in Fig. 2 and Fig. 3 discussed so far demonstrate that *Dichography* can deal with markedly different shapes and sizes between the two retrieved frames. An additional relevant feature of single-particle CDI experiments at XFELs are the fluctuations in the brightness of the diffraction signals. In fact, samples are intercepting the light pulse while free-flying, and their position in the focus at the diffraction event is ruled by statistics. Particles can intercept the light pulse at varied positions in the focal volume, with distinct light intensity and, consequently, diffraction brightness. This is further enhanced by intensity fluctuations in the XFEL source.

It is straightforward to deduce that, in the “double-hit” case, two particles far apart in the interaction region can be subjected to different pulse intensities, causing both deviations in the overall brightness as well as unbalance in the scattering contribution between the two frames. Less intuitively, this is also a key feature in the *two-color* case, due to the different positions of the foci of the two pulses, as discussed in the next section (see Sec. D 2 for technical details). These factors must be considered when evaluating the imaging performance of *Dichography*.

Imaging results on double silver nanoparticles provide a valuable opportunity to comment on the method’s performance in this regard. In particular, brightness balancing can be estimated for successful reconstructions, for which we can separate the individual contributions to the scattering signal (as shown in Fig. 2d and 2e). For the example reported in Fig. 2, the ratio between the total number of recorded photons is very close to one, with the first frame (Fig. 2b) yielding just 35 % more photons than the second one (Fig. 2c). The asymmetry in scattered photons increases significantly for other cases. The number of photons scattered by the first frame in Fig. 2c turns out to be 3.3 times higher than the second one, while the ratio goes up to a factor 3.8 times for the reconstruction in 2b.

The sensitivity of the method to an imbalance of scattered photons between the two frames, while partially related to the morphological properties of the samples, strongly depends on the overall brightness of the recorded signal and arises from the dependence of noise on the field intensity. In general, a higher photon yield in the signal allows for *dichographic* reconstructions with a stronger intensity imbalance between the two frames. Further discussion, supported by tests on simulated data, is provided in Sec. S1 of the Supplemental Material [34].

The results on “double-hits” discussed so far, while being of limited scientific interest, represent a strong demonstration of the viability of *Dichography* for significantly differing morphologies and sample properties. These data is characterized by optimal brightness conditions, with the XFEL operating around its maximum performance in terms of total power per pulse and intensity in the focus. These results represent a solid ground

for the discussion of the following dataset, which has a high scientific relevance but poses major challenges due to the advanced operational mode of the XFEL.

### B. The ultrafast movie of xenon-doped helium nanodroplets

The analysis of diffraction patterns produced by two-color XFEL light pulses is the fundamental motivation behind the development of *Dichography*. The two light pulses, interacting at different times with the sample, imprint its time evolution in the diffraction signal. The two *views* on the sample are reconstructed by *Dichography* to gain a full-fledged two-frame movie. However, this intriguing potential comes along with technical challenges, as discussed in the following.

The experiment was performed at the European XFEL facility, taking advantage of the recently available capability of producing two collinear X-ray pulses of different radiation wavelengths with controllable time delays delay [19]. The two co-propagating pulses are tuned to 1.0 keV and 1.2 keV photon energy, corresponding to 1.2 nm and 1.0 nm wavelength, and are separated in time by 750 fs. Both are focused in the interaction region, where they intercept isolated superfluid helium nanodroplets doped with xenon. An individual droplet in the focus interacts with both pulses, and the corresponding scattered fields incoherently overlap on the detector. Further details on the experiment are discussed in Appendix D 2.

Two diffraction images acquired in these conditions are shown in Fig. 4a and Fig. 4d. A relevant feature of these patterns is the low number of photons recorded by the detector, if compared to the photon yield for the standard, single pulse, operation mode of the XFEL [35] (see Appendix D 2). This aspect represents a challenge for a photon-hungry technique such as CDI, and thus even more so for *Dichography* (as further investigated in Sec. S1 of the Supplemental Material [34]).

Nevertheless, the specific properties of the physical system under study, i.e. doped superfluid helium nanodroplets, allow us to take advantage of the Droplet Coherent Diffraction Imaging (DCDI) approach [36]. The DCDI method constrains the underlying helium droplet structure during the actual reconstruction process. The droplet size and brightness are extracted in the pre-processing phase, by fitting the experimental data with the diffraction profile of a spherical sample. The information to be retrieved, therefore, pertains solely to the internal structure of the doping material. For conventional CDI, this greatly reduces the complexity of the problem, it increases the convergence properties of the algorithms compared to standard CDI, and it makes the reconstruction process much more resilient to noise [36].

The DCDI method has been incorporated into the *Dichography* reconstruction process through a straightforward adaptation of its original workflow, as discussed in Appendix E, and is used here to analyze the two-color

diffraction images presented in this section. Its applicability to this dataset relies on the possibility of extracting the droplet size as well as on the persistence of the pristine helium droplet density, embedding the xenon doping, up to a time delay of 750 fs. Both aspects are investigated and verified using pure-helium data acquired during the same experimental campaign, as reported in Ref. [35].

Despite the demanding experimental conditions, the reduction in problem complexity achieved through the use of DCDI makes these two-color data barely tractable with *Dichography* in a few optimal cases. The two frames reconstructed from the diffraction pattern shown in Fig. 4a are presented in Fig. 4b for the 1.0 keV pulse, and in Fig. 4c for the following 1.2 keV pulse. The 1.0 keV reconstruction in Fig. 4b reveals a continuous structure extending from the center of the helium droplet to its lower boundary. This feature is consistent with previous observations of xenon atoms aggregating along quantum vortices in superfluid helium [36–38].

A similar structure is also observed in the 1.2 keV reconstruction shown in Fig. 4c, indicating consistency between the two measurements. However, beyond this replicated feature, notable differences are present. In particular, the 1.0 keV reconstruction exhibits a high-density spot on the left side of the droplet, which is absent in the 1.2 keV reconstruction. Conversely, the 1.2 keV reconstruction displays a distinct high-density spot at the lower-right edge of the droplet, with no corresponding feature in the 1.0 keV image.

Analogous observations are obtained from the reconstructions obtained from the pattern in Fig. 4d. In particular, here all the high-density regions due to the presence of xenon retrieved in the 1.2 keV reconstruction in Fig. 4f can be linked with corresponding features in the 1.0 keV reconstruction in 4e. In the earlier 1.0 keV frame, however, additional features are visible due to an overall lower signal-to-noise ratio.

The observable differences in terms of reconstruction features and quality between the two patterns, Fig. 4a and Fig. 4d, can be further discussed in terms of the properties of the diffraction signal. First of all, the overall scattering signal is 80 % stronger in the former case.

A second relevant aspect deals with the relative brightness between the 1.0 keV and the 1.2 keV pulses within the single diffraction image. In fact, the foci of the two different pulses produced by the FEL have only a partial overlap in space along the propagation direction, due to the different source points of the two colors, produced upstream at different undulators sections. As a consequence, the individual particles can be subjected to significantly different photon densities of the two FEL pulses, depending on their position in the interaction region (see Appendix D 2). Concerning the first case in Fig. 4a, the number of photons scattered by the 1.2 keV pulse is 64 % larger than those coming from the interaction with the 1.0 keV pulse. This is significantly more unbalanced for the second example in Fig. 4d, for which the photons scattered by the 1.2 keV pulse are close to

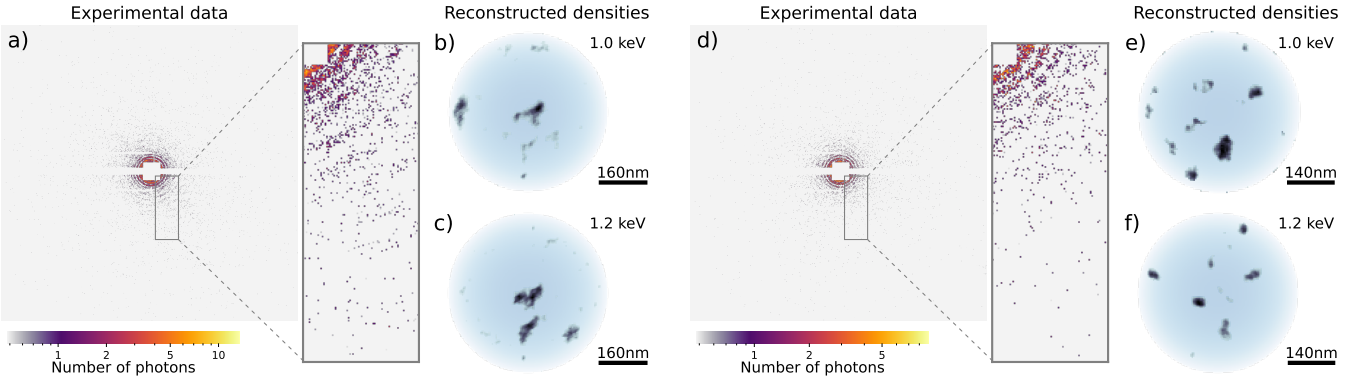


FIG. 4. Reconstructions from two-color diffraction patterns acquired at the European XFEL, produced by superfluid helium nanodroplets doped with xenon. Two experimental diffraction patterns are reported in a) and d), on which the diffraction signals produced by two different photon energies, 1.0 keV and 1.2 keV, are superimposed. The intensity is encoded as reported by the color bar at the bottom. The intensity values are translated into numbers of 1.2 keV photons per pixel. The inset plot is a zoomed-in region of the diffraction image, to better appreciate the photon statistics, and thus the statistical noise, that affects the experimental data. The two reconstructed frames of the electronic density are reported in b), c) and e), f) for the patterns in a) and d), respectively. In particular, b) and e) report the reconstruction from the 1.0 keV pulse, while c) and f) correspond to the 1.2 keV pulse, hitting the target 750 fs later. The reconstructed density of the xenon doping follows the color bar in Fig. 3. The shape of the helium droplets, independently retrieved before the imaging process and constrained using the DCDI method, are superimposed in blue color.

3 times more abundant than those from the 1.0 keV one. This renders the reconstruction more challenging and significantly impacts the signal-to-noise ratio of the 1.0 keV reconstruction in Fig. 4e.

From the representation of the retrieved densities in Fig. 4, the reader may question whether the similar structures in the two frames arise merely as a *ghosting* artifact – i.e., features from one frame being mistakenly replicated in the other. However, the use of different radiation wavelengths in *two-color* diffraction data intrinsically implies that the sample is imaged with different spatial resolutions in the two frames. Specifically, the spatial extent corresponding to a single pixel varies between the frames, becoming smaller at higher photon energies due to the increased resolution at a shorter wavelength. As a result, the same structure spans a different number of pixels in the two reconstructions, and appears visually similar in size only when both are displayed with a common scale bar, as done in Fig. 4. This point is further illustrated in Fig. 7 and discussed in more detail in Appendix E. *Ghosting* in *two-color Dichography* would then give rise to a replicated structure but with a different scaling. Thus, its presence can be excluded for the xenon structures observed in Fig. 4.

The presence of the same structure in both *frames*, apart from the artifacts discussed above, implies that the xenon agglomerates survive for at least 750 fs after irradiation with the *pump* pulse. This observation is, however, limited by the achieved spatial resolution of about 20 nm, which is set by the maximum momentum transfer at which the scattering signal remains above the noise level [35].

#### IV. DISCUSSION

In this work, we introduce the *Dichography* method to perform Coherent Diffraction Imaging (CDI) in cases where two non-interfering diffraction signals overlap on the detector. This method finds direct application in *two-color* experiments at XFELs, where pairs of ultra-short pulses with controllable time delay and different wavelengths can be generated. *Dichography* enables the reconstruction of two independent frames, corresponding to the two distinct *views* of the system provided by the different colors—thus unlocking the possibility of producing a full-fledged movie of the sample.

The applicability of *Dichography* extends beyond the two-color case, as it generally applies to any scenario where the recorded diffraction data is the incoherent sum of two independent signals. The so-called “double-hit” case, where two particles, spatially separated in the interaction region, are simultaneously illuminated by a single light pulse, is one such scenario and serves as a benchmark for the method.

In this case, *Dichography* enables the separation of the scattering contributions and the retrieval of the corresponding densities of the two particles within the focal volume in two separate frames. The various provided examples (see Fig. 2 and Fig. 3) cover a wide range of cases in terms of sample shape, spatial extent and brightness of the two scattering signals. They serve as practical demonstrations that, in principle, no prior knowledge about the samples is required, nor are any specific constraints imposed on the relationship between the properties of the two retrieved frames.

The only assumption about the samples is the *over-*

*sampling* condition, similarly to conventional single-particle CDI – namely, the isolated nature of the nanoparticle in a zero-scattering background. Mathematical considerations suggest that the necessary extent of the surrounding zero-scattering region, known as *oversampling degree*, is more restrictive for *Dichography* than for conventional CDI, as further investigated in Appendix B. While the existence of a unique reconstruction is demonstrated for conventional CDI, it is supported by practical evidence in the case of *Dichography*, and it is yet to be proven. This aspect is discussed in details in Appendix B 1.

The brightness of the patterns and the distribution of the photons between the two frames become significantly more restrictive for the *two-color* imaging case, were the two overlapping fields come from two XFEL pulses at different photon energies. Here, the special mode of operation of the XFEL undulators delivers two light pulses with significantly reduced intensity with respect to standard operation mode [19], as further discussed in Appendix D 2. Therefore, the reconstructions of xenon-doped superfluid helium nanodroplets shown in Fig. 4 are only possible by employing the DCDI method [36], which is restricted to samples embedded in nanoparticles with known shape and low scattering cross-section – so far only demonstrated for the specific case of superfluid helium nanodroplets [39]. The employment of the DCDI approach greatly reduces the problem complexity and makes the reconstruction process significantly more resilient to noise. Even so, only specific patterns with optimal condition, i.e. higher brightness and similar photon yields between the two frames, turn out to be tractable. Tests on simulated *two-color* diffraction images, discussed in Sec. S1.4 of the Supplemental Material [34], suggest, however, that even just a twofold increase of the diffraction intensity can lead to a stunning improvement in the reconstruction quality and reliability.

*Dichography*, similar to conventional single-particle CDI, is an *indirect* imaging technique, as the sample image has to be retrieved algorithmically from the measured data [6, 7]. The algorithmic approach at the core of *Dichography* is built on a direct, relatively straightforward, adaptation of the algorithms for single-shot CDI, as discussed in Appendix A. The higher complexity of the *dichographic* problem and its peculiarities render the algorithm less effective in the reconstruction process. Therefore, the imaging performance is boosted by the combined use with an *evolutionary algorithm*, which already demonstrated superior performance and reliability for conventional single-particle CDI [40], as further discussed in Appendix C. A more rigorous and fundamental understanding of the problem, which substantially differs from conventional CDI in some key aspects, could result in the design of more efficient imaging algorithms and analysis workflows, extending the range of applicability even further.

## V. OUTLOOK

The implications of the successful demonstration of *Dichography* extend significantly beyond the physical observations and the overall quality of the two-frame reconstructions discussed in this work. In fact, the practical realization of two-frame CDI from overlapping scattering signals can serve as a strong driver for further improvements in the two-color mode of XFELs, e.g. toward higher intensities. Furthermore, it could act as a catalyst for original experimental concepts and designs in several directions that were previously considered nonviable for imaging approaches.

Another modern operational mode of XFELs allows for the generation of light pulses with sub-femtosecond durations [1–5, 33, 41]. The combination of these *attosecond* pulses with diffraction imaging has already demonstrated the ability to access ultrafast ionization dynamics by exploiting transient electronic resonances [42]. Recently, *attosecond* pulses have been combined with the *two-color* mode [1]. Thanks to the short time duration of the pulses, which can outrun the lifetime of excited electronic configurations, *two-color attosecond Dichography* may provide unprecedented insights into such elusive states, like the lifetimes, spatial distribution and evolution of electronic excitations [43, 44] or plasmonic phenomena such as charge density waves in complex nanostructures, depending on their size, shape and surrounding environment.

Two-color X-ray *Dichography* can be effectively combined with the use of a third pulse from an optical laser to enable a completely new class of imaging experiments. The laser can be employed to trigger a metastable state, which temporarily opens a specific transition triggered with the XFEL *pump* and tracked by the XFEL *probe*. The two consecutive XFEL pulses can also be employed as a *double probe*. For example, nanoparticles can be superheated by a laser, leading to fast out-of-equilibrium dynamics, like shock-waves and disintegration of the sample [18]. The laser irradiation is followed by the two consecutive XFEL pulses. *Dichographic* reconstructions are thus two snapshots of the evolving system that allow to precisely track its kinematics and the dynamics of the molecules.

While the current performance of *two-color* pulses turns out to be challenging for *Dichography*, recent works have demonstrated the capability of partially separating individual photons between the two pulses. This is achieved by exploiting the sensitivity of the detector to the photon's energy combined with advanced analysis techniques [35]. The feeding of this additional information into the algorithmic workflow of *Dichography* is currently under development. Enhancements in the quality and reliability of the reconstructions are expected and they will be the subject of future work.

Improvements of XFELs in *two-color* mode, in terms of pulse brightness, are also expected in the next years, thanks to the developments of XFEL technology encour-

aged by the increasing interest of the scientific community [45]. However, even with the current performance, the brightness of the scattering signal can be boosted in different ways. The xenon-doped helium nanodroplets analyzed in this work have an intrinsically low scattering cross section [46]: the highly-scattering xenon represents only a small fraction of the whole system, thus contributing only marginally to the scattered field. An overall diffraction signal even orders of magnitude higher is expected for systems with significantly higher cross sections, e.g. heavier elements. Furthermore, markedly larger scattering cross sections even for lighter materials can be attained at lower photon energies, from few tens to few hundreds of eV [47, 48]. This energy regime in-between the extreme ultraviolet and soft X-ray is also characterized by the presence of electronic resonances for different elements [49], like the biologically relevant carbon and oxygen, where ultrafast electron dynamics can be triggered [42] and traced thanks to the strong variations in the scattering cross section [50].

A further experimental domain that can benefit from the imaging capabilities of *Dichography* is the study of physical systems sensitive to light polarization. Indeed, several XFEL light sources can partially [51] or fully [52] tune and control the polarization properties of the light in both the XUV [53] and X-ray spectra [54], even with ultrashort light pulses [55]. Moreover, *two-color* pulses with controllable time-delays and independent polarizations have been recently demonstrated [24]. *Dichography* can be combined with these experimental capabilities to study the spatial distribution and time evolution of *dichroic* systems – i.e., systems whose scattering response is sensitive to light polarization. Among these, magnetic domains [56], molecular chirality [57], and orbital ordering in crystals [58] are highly active research topics.

While the difference in wavelength between the two pulses is effective for a better spatial separation of the signal on the scattering detector, it is not a fundamental requirement for *Dichography*. Thus, if significant structural modifications are expected to take place in the sample between the two XFEL pulses [31], the same photon energy can be potentially employed. This feature would allow the whole set of XFEL undulators to be tuned to the same wavelength, and thus the full peak power to be reached. However the development of methods to produce pairs of electron bunches with sub-picosecond controllable time delay is required to gain full advantage from such an experimental scheme.

*Dichography* represents a major step forward in harnessing the imaging capabilities of *two-color* light pulses emerging at XFEL facilities. Indeed, the two *views* on the sample at different points in time embody, in every respect, one of the original promises of X-ray Free Electron Lasers: recording ultrafast movies of nanomatter.

## Acknowledgments

The research leading to these results was supported by SNSF project 10003697 “Visualizing coherent and collective electron dynamics in nanoscale matter” and the COST Action CA21101 “Confined Molecular Systems: From a New Generation of Materials to the Stars (COSY)”. We acknowledge the Paul Scherrer Institute, Villigen, Switzerland for provision of free-electron laser beam time at the Maloja instrument of the SwissFEL ATHOS branch and thank the SwissFEL staff for their assistance. We acknowledge the European XFEL in Schenefeld, Germany, for the provision of X-ray free-electron laser beam time at the SQS instrument and thank the EuXFEL staff for their assistance. TF and CP acknowledge funding by the Deutsche Forschungsgemeinschaft within CRC 1477 ”Light-Matter Interactions at Interfaces” (project number 441234705). We thank the IT Services Group (ISG) of the Department of Physics at ETH Zurich for the excellent support and management of the computing hardware employed for this research.

## Author contributions statement

LH, BB, TB, SDe, ADF, SDo, TF, RH, SK, BK, AOL, BL, SM, TM, MMe, CP, TP, BS, KSi, FSt, RMPT, PT, SU, YO, MMu, DR and AC contributed in the planning and conduction of the experiment at the SQS instrument of the European XFEL (ID 2857). The experiment was led by MMu and YO. LH, AAH, JB, CB, SDo, TF, FG, CG, GJ, MJ, GK, KK, CP, SR, AS, MS, FSc, KSc, ZS, PT, CFU, VW, XX, MY, OY, NY, HZ, BvI, DR and AC contributed in the planning and conduction of the experiment at the Maloja endstation of SwissFEL (ID 20222035). The experiment was led by BvI and DR. SD, JB and SR curated the sample delivery, whose performance allowed for the systematic recording of double-hits. AC developed the original algorithmic approach to *Dichography* and its numerical implementation. AC and DR analyzed the performance of the method on simulated data and “double-hit” patterns from the SwissFEL experiment. LH pre-processed the two-color data from the European XFEL experiment, took care of the data selection and developed and implemented the size and shape determination of the helium nanodroplets. AC and LH adapted the DCDI method for *Dichography* and conducted tests on simulated and experimental data. AC, LH and DR contributed in the writing of the manuscript, with input and feedback from all coauthors.

## Data and code availability

The imaging software employed to produce the results presented here is hosted at <https://gitlab.ethz.ch/nux/equinox>, along with examples on simulated and experimental data. Data recorded for the experiment at the European XFEL are available at [doi:10.22003/XFEL.EU-DATA-002857-00](https://doi.org/10.22003/XFEL.EU-DATA-002857-00).

## Appendix A: Algorithmic approach to Dichography

### 1. Iterative phase retrieval

Coherent Diffraction Imaging (CDI) is an *indirect* imaging method that requires extensive numerical analysis to obtain the sample image from the recorded data. The scattered field  $\psi$  encodes the complete information about the spatial density of the sample,  $\rho$ , as they are mathematically linked by a Fourier Transform (FT) operation (under certain approximations [7]). It is therefore possible to reconstruct  $\rho$  from the full knowledge of the field, i.e.,  $\rho \propto \mathcal{F}^{-1}[\psi]$  where  $\mathcal{F}^{-1}$  indicates the inverse FT operation. However, the experimentally recorded image,  $I$ , provides information only on the field's amplitude, i.e.,  $I \propto |\psi|^2$ , while the field's phase is lost. Recovering this lost phase corresponds to reconstructing the sample density  $\rho$ . This so-called *phase retrieval problem* lies at the core of CDI analysis and must be solved by suitable numerical approaches.

Conventional algorithms for phase retrieval, such as the Hybrid Input-Output (HIO) and Error Reduction (ER) methods [59], are characterized by an *iterative* scheme, as they cyclically impose two constraints [32]. On one hand, the *oversampling* condition is enforced by setting to zero the density values outside the spatial extension of the sample. This is achieved by defining a *support* function, a binary-valued matrix whose entries are set to 1 where non-zero density of the sample is expected, and to 0 where zero scattering is enforced. On the other hand, the intensity constraint is applied in reciprocal space, where the experimentally measured intensities replace the Fourier amplitudes of the current density estimate. This iterative approach is retained for *Dichography* and lies at the core of the numerical retrieval of the two frames,  $\rho^A$  and  $\rho^B$ .

Fig. 5 shows a flowchart of the iterative phase retrieval algorithm adapted to *Dichography*. It comprises two reconstruction workflows, one for each *frame*, visually separated on the left and right sides of Fig. 5. Each workflow follows the typical scheme of conventional iterative algorithms [32, 59]. Both densities,  $\rho^A$  and  $\rho^B$ , are independently initialized, typically with random values, and each is constrained to its own support function in real space,  $s^A$  and  $s^B$ , respectively. However, unlike conventional CDI, the two procedures are entangled when constraining the experimental intensities in Fourier space. This step is shown at the center of Fig. 5.

For each coordinate  $i, j$  in Fourier space, the sum of the squared amplitude of the scattered fields  $\psi^A$  and  $\psi^B$  is constrained to the acquired intensities  $I$ , i.e.:

$$|\psi_{ij}^A|^2 + |\psi_{ij}^B|^2 \stackrel{!}{=} I_{ij}. \quad (\text{A1})$$

The way in which this is numerically enforced and propagated to the two individual reconstructions is discussed in the next subsection.

### 2. Constraining experimental data

In *Dichography*, the experimentally acquired information on the sum of the two scattering signals has to be constrained, i.e., propagated to the two frames of the reconstruction, to make the two estimates of the field,  $\psi^A$  and  $\psi^B$ , satisfy the condition in Eq. (A1).

An intuitive description of the operation is reported in Fig. 6. For a given pixel coordinate  $i, j$ , the values of the scattered fields  $\psi_{ij}^A$  and  $\psi_{ij}^B$  can be represented in the complex plane, as in Fig. 6a, in polar coordinates. The two moduli,  $M^A$  and  $M^B$ , can then be considered as the two components of a two-dimensional vector, as shown in Fig. 6b. The condition in Eq. (A1) can be achieved by a *renormalization* of the vector  $(M^A, M^B)$  to obtain a new vector  $(M'^A, M'^B)$  whose norm corresponds to the square root of the experimental data,  $\sqrt{I}$ , while its phase  $\phi^M$  is preserved. The rescaled moduli  $M'^A$  and  $M'^B$  replace the original ones in the two field estimates, as shown in Fig. 6c, while the field phases  $\phi^A$  and  $\phi^B$  are retained. Once the operation is repeated for all entries in the matrix, the experimental constraint is fully *back-propagated* to the two frames of the reconstruction.

Unlike conventional CDI – in which only a single phase needs to be recovered for each field amplitude – the *phase retrieval problem* in *Dichography* is three-fold. Indeed, it requires the recovery of three phase values:  $\phi^A$  and  $\phi^B$  for the two scattered fields, as well as  $\phi^M$ , which encodes the relative fields amplitude.

Differently from conventional CDI – where for each field amplitude only a single phase has to be recovered –, the *phase retrieval problem* in *Dichography* is three-fold, requiring the retrieval of three phase values,  $\phi^A$  and  $\phi^B$  for the two scattered fields and  $\phi^M$  that encodes their relative amplitude.

A detailed and formal presentation of the mathematical operations involved is provided in Sec. S3 of the Supplemental Material [34].

The most common iterative phase retrieval algorithms share the same way of constraining Fourier intensities, while they differ in the application of the support constraint. The modified intensity constraint described in Fig. 6 can thus be directly implemented in all conventional iterative phase retrieval algorithms [32, 59]. The behavior of the algorithms, however, differs from their conventional CDI counterparts due to the different mathematical nature of the underlying optimization problem (as discussed in Sec. S4 of the Supplemental Material [34]).

Conceptually similar implementations of this intensity constraint have been developed and employed to deal with broadband diffraction data, in cases where the spectral information is known [60, 61], or even where the spectrum of the scattered light is retrieved along the reconstruction process [62]. These approaches have opened new possibilities for CDI with broadband or polychromatic pulses, like those delivered by High-Harmonic Generation sources [63]. Still, differently from those meth-

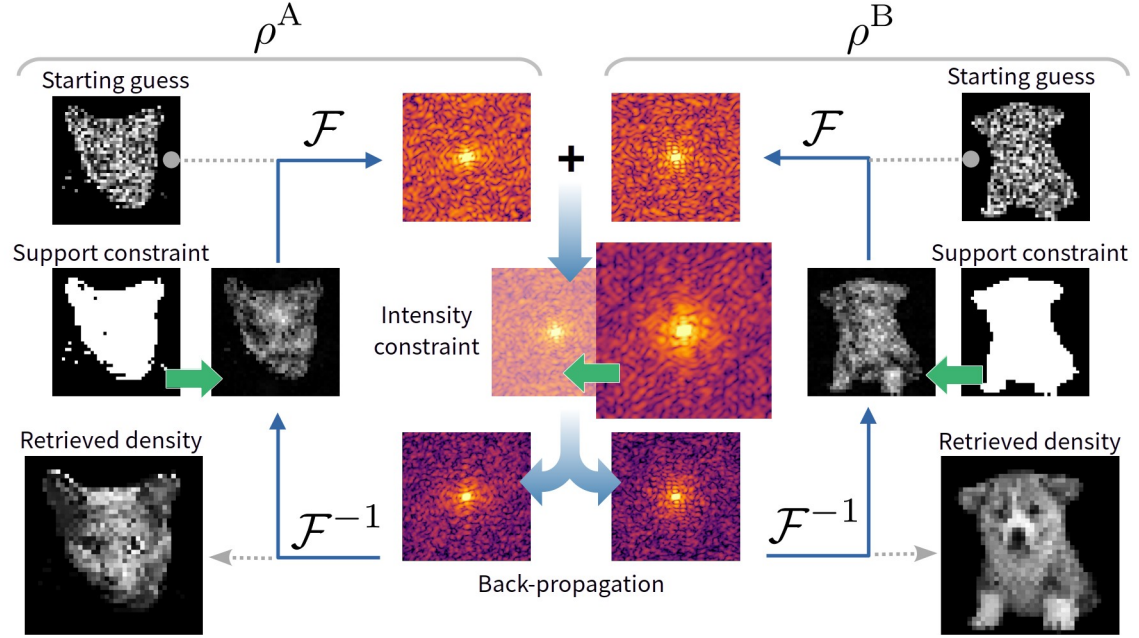


FIG. 5. Scheme of the iterative phase retrieval algorithm for *Dichography*. The approach corresponds, in most steps, to the execution of two independent reconstruction procedures,  $A$  and  $B$ , using conventional iterative phase retrieval algorithms. The two densities,  $\rho^A$  and  $\rho^B$ , are randomly initialized. Two constraints – the support function in real space and the experimental intensities in Fourier space – are cyclically enforced. The application of the real-space constraint (shown on the right and left sides of the figure) is independent for  $A$  and  $B$ , each with its own support function. This step is thus equivalent to conventional methods for two independent reconstructions. The Fourier intensity constraint, depicted in the center of the figure, is shared between  $A$  and  $B$ . Here, the sum of the two Fourier amplitudes is replaced by the experimentally measured values. This information is then back-propagated to the two separate densities,  $\rho^A$  and  $\rho^B$ . The two reconstruction outcomes are returned once the total number of iterations is reached. For sake of clarity, the knowledge of the correct support functions is assumed *a priori*. However, in all reconstructions presented in this work, the supports are unknown and recovered along the reconstruction process, as discussed in Appendix A 3.

ods, *Dichography* doesn't enforce any structural connection between the contributions to the recorded scattering signals. This allows capturing structural changes in the samples, as discussed in the following section.

### 3. Real-space constraint

The application of the real-space constraint, i.e., the support function, is performed independently on the two frames, as if they were two separate reconstruction procedures using iterative algorithms for conventional single-particle CDI. This means that each of the two densities,  $\rho^A$  and  $\rho^B$ , is constrained to its own independent support function,  $s^A$  and  $s^B$ , respectively, as shown in Fig. 5. The way the support constraint is enforced depends on the specific iterative algorithm employed [32] and retains its form in the adaptation for *Dichography*.

A similar consideration applies to the retrieval of the support function itself. A fundamental problem in single-particle CDI is the definition of the support function, which is, in most cases, not known *a priori*. The *Shrink-wrap* algorithm (SW) [28] has proven to be a fundamental tool for retrieving the correct support function without

prior knowledge of the sample. The SW algorithm refines an initially loose support estimate during the reconstruction process, as described in Ref. [28]. Here, the SW algorithm is employed in its original form to independently retrieve the support functions of the two densities,  $\rho^A$  and  $\rho^B$ . All *Dichography* results presented in this work used the SW algorithm to determine the samples' spatial extent, and no *a-priori* information about the particle shape was employed.

### Appendix B: Oversampling requirements for Dichography

The *oversampling* condition is strictly necessary in CDI [6, 32] and it requires the sample density to be surrounded by a region of known scattering density. For single-particle CDI, this condition is enforced by the support function which constraints zero-scattering outside of the sample.

The recorded data gives information only on the amplitude  $|\psi_{ij}|$  of the Fourier representation of the scattering density  $\rho$ , as the phases are lost. The *oversampling* condition thus introduces redundancy in the recorded am-

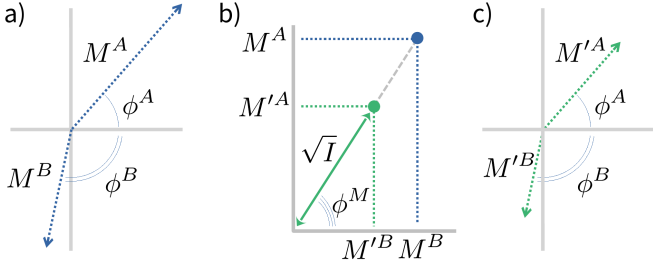


FIG. 6. Graphical representation of the action of the *intensity projector* as implemented for *Dichography*. In a), the amplitude  $M$  and phase  $\phi$  of the two reconstructed fields  $\psi_{ij}^A$  and  $\psi_{ij}^B$  are represented in the complex plane. In b), the two amplitudes  $M^A$  and  $M^B$  can be interpreted as the components of a two-dimensional vector, whose norm is rescaled to match  $\sqrt{I}$ , where  $I$  is the acquired experimental data. In c), the rescaled amplitudes  $M'^A$  and  $M'^B$  replace the original ones, while the phases  $\phi^A$  and  $\phi^B$  are retained. This representation of the intensity constraint makes it clear that, for each value of the experimental data  $I_{ij}$ , three phases must be retrieved,  $\phi^A$ ,  $\phi^B$  and  $\phi^M$ , in contrast with a single one in conventional CDI.

plitudes which allows them to also encode phase information. For conventional CDI, the amount of information redundancy provided by the recorded intensities  $I$  is evaluated through the *oversampling degree*  $O_d$ , defined as [64]:

$$O_d = \frac{\text{total number of pixel}}{\text{number of pixel to retrieve}} = \frac{N \times N}{\sum S_{ij}} \quad (B1)$$

where  $N$  is the linear dimension of the square matrix containing the recorded diffraction data  $I$  and  $S$  is the binary function that identifies the *support*. It has values  $S_{ij} = 0$  for those coordinates where the zero-scattering region is enforced, and  $S_{ij} = 1$  where the the density values have to be retrieved.

It has been shown that the minimum *oversampling* requirement for conventional CDI is  $O_d > 2$ , to keep the number of “equations” (the number of recorded intensities  $N \times N$ ) higher than the number of “unknowns” (twice the *support* size, as each retrieved pixel belongs to  $\mathbb{C}$ ). This condition can be interpreted directly in reciprocal space: only the amplitudes of the Fourier representation are accessible as  $\sqrt{I_{ij}}$ , but twice the amount of information has to be retrieved, i.e. the module  $|\psi_{ij}|$  and the phase  $\arg[\psi_{ij}]$ .

In the case of *Dichography*, different  $O_d$  conditions are required, due to the higher number of unknowns to be retrieved. To better investigate this requirement, it is necessary to re-define the *oversampling degree* to take

into account that two densities  $\rho^A$  and  $\rho^B$  are retrieved:

$$O'_d = \frac{\text{total number of pixel}}{\text{number of pixel to retrieve}} = \frac{N \times N}{\sum S_{ij}^A + \sum S_{ij}^B} \quad (B2)$$

where  $S^A$  and  $S^B$  are the matrices encoding the support functions of the two frames  $\rho^A$  and  $\rho^B$ .

As discussed in Sec. A 2, *Dichography* replaces the squared sum of the two scattering amplitudes with the experimental data  $I$ . As schematically reported in Fig. 6, for each entry  $i, j$  in the matrix, the estimates of the phases for the two fields,  $\phi^A$  and  $\phi^B$  are retained. Furthermore, the rescaling operation of the two amplitudes to match the experimental data can be interpreted as a renormalization of a vector, where its phase  $\phi^M$  is also retained.

Overall, for each recorded intensity  $I_{ij}$ , three phases have to be retrieved – compared to the single phase value for conventional CDI –  $\phi^A$  and  $\phi^B$  and  $\phi^M$ , where the latter encodes the relative amplitude of the two signals. This consideration leads to the conclusion that the minimum condition of the *oversampling degree* that allows for *Dichography* is  $O_d > 4$ .

By inserting the condition into Eq. (B2), the following condition can be derived:

$$\sum S_{ij}^A + \sum S_{ij}^B < \frac{N^2}{4} \quad (B3)$$

i.e., the sum of the areas of the two supports  $S^A$  and  $S^B$  has to be less than a fourth of the whole matrix. For similarly extended frames (i.e. with similar support size), the individual densities  $\rho^A$  and  $\rho^B$  cannot extend more than  $1/8$  of the whole matrix area, a significantly more restrictive condition than the  $1/2$  for conventional CDI.

## 1. Uniqueness of the solution

All imaging algorithms for conventional CDI are, in practice, optimization algorithms [7, 32, 40]. They are designed to minimize the difference between the measured experimental data and the Fourier intensities of the reconstructed sample image. Thus, the *phase retrieval problem* is an *optimization problem*. The reconstruction  $\rho$  produced by *phase retrieval* algorithms can then be regarded as the *solution* to the imaging problem. For conventional CDI, it has been demonstrated that the solution is *unique* – i.e., there exists only one specific sample image that can produce the measured scattering signal – up to a restricted set of ambiguities that can be trivially resolved, such as translation in space or a  $180^\circ$  rotation [7].

The existence of a unique solution for *Dichography* remains an open question, as a formal mathematical proof is still lacking. We encourage further investigations in

this direction, supported by a more rigorous mathematical treatment of the *dichographic* imaging problem.

Still, we are convinced about the consistency of the imaging results obtained with *Dichography*. On the one hand, extensive tests on simulated data have never shown cases in which the reconstructed *frames* exhibited significant deviations from the expected solution – aside from the detrimental effects of noise, as extensively investigated in Sec. S1 of the Supplemental Material [34].

On the other hand, the uniqueness of the solution can be deduced for a specific case – by comparing the *dichographic problem* with the conventional *phase retrieval problem* – and it could serve as a starting point for a complete mathematical demonstration. As discussed in Sec. II, the recorded signal  $I$  is the incoherent sum of two scattered intensities, i.e.,  $I = I^A + I^B$ , where  $I^A$  and  $I^B$  correspond to the diffraction signals of the densities in the two frames,  $\rho^A$  and  $\rho^B$ .

If one of the two frames, e.g.,  $\rho^A$ , is correctly retrieved, this implies full knowledge of  $I^B$ , as

$$I^B = I - |\mathcal{F}[\rho^A]|^2, \quad (\text{B4})$$

where  $|\mathcal{F}[\rho^A]|^2$  is the retrieved intensity  $I^A$ . Eq. (B4) reduces to a conventional phase retrieval problem for the frame  $\rho^B$ , whose uniqueness is known. This means that if one frame is correctly retrieved, the other frame has only a unique solution in the *dichographic problem*.

### Appendix C: Adaptation of Memetic Phase Retrieval

The capability of iterative phase retrieval algorithms to reach the *solution* to the phase retrieval problem – i.e., to correctly reconstruct the sample density – is a key factor in CDI. These algorithms are, in fact, the *virtual lenses* of CDI, and the quality and reliability of the retrieved sample image are heavily dependent on their performance. For this reason, significant effort has been devoted to the development of various iterative algorithms [32]. These algorithmic approaches are well established and are routinely employed in CDI-based experimental techniques at synchrotrons, such as *Bragg-CDI* [65] or *Ptychography* [66].

Single-particle single-shot CDI performed at XFELs comes, however, with additional complications that render the algorithm’s task non-trivial. For example, the central region of the diffraction pattern cannot be recorded due to the presence of a hole in the detector, necessary to prevent damages from the transmitted beam. Furthermore, the brightness of the patterns is most of the time sub-optimal and cannot be increased, as the intensity of the single XFEL pulse is already tuned to its maximum performance. These factors significantly impact the performance of iterative algorithms and render CDI at XFELs considerably more challenging.

A recent breakthrough in algorithmic capabilities comes from the development of the Memetic Phase Retrieval (MPR) approach [40, 67]. This approach takes advantage of the parallel execution of several reconstruction procedures on the same diffraction pattern. Information between these reconstructions is shared through a genetic algorithm, which augments the capabilities of conventional iterative algorithms and boosts the quality and reliability of the image reconstruction [40].

Mathematical considerations (see Appendix B) as well as systematic tests on simulated data (see Sec. S1 and Sec. S4 of the Supplemental Material [34]) show that *Dichography* reconstructions are more demanding than conventional CDI, and that the performance of conventional iterative algorithms is further impacted. Thus, the MPR scheme has been adapted to *Dichography*, resulting in a significant boost in performance.

The MPR adaptation for *Dichography* is called *Equinox*. *Equinox* has been employed to obtain all imaging results presented in this manuscript, as well as those on simulated data discussed in the Supplemental Material, unless specified otherwise. It is implemented as a Python package directly derived from the SPRING software [40], a recently released toolset for image reconstruction in conventional single-particle single-shot CDI. The open-source implementation of *Equinox* and its documentation are accessible at <https://gitlab.ethz.ch/nux/equinox>.

## Appendix D: Experimental details

### 1. Silver nanoparticles at SwissFEL

The two-color experiment was performed at the Maloja endstation of SwissFEL [68, 69]. Wet-chemically grown silver nanoparticles were injected into the experimental chamber, kept under vacuum conditions, using an electrospray and a set of aerodynamic lenses [70, 71]. The electrospray disperses the liquid containing the dissolved nanoparticles into sub-micron-sized droplets. The nanoparticle concentration is optimized for a single sample per droplet. The droplets flow toward the interaction region along with a buffer gas in a set of aerodynamic lenses, where the liquid evaporates.

The XFEL pulses, with a duration of 50 fs and a total energy of 3 mJ, are delivered by SwissFEL at a repetition rate of 100 Hz. The pulses are tuned to a photon energy of 1000 eV, corresponding to a wavelength of 1.24 nm, and intercept the nanoparticles in a 3  $\mu\text{m}$  focus. These parameters correspond to a maximum intensity in the focus of approximately  $10^{18} \text{ W/cm}^2$ . The scattering signal is recorded by a 4-megapixel *Jungfrau* detector optimized for soft X-ray photon detection [27, 72]. The detector placement allows for the detection of the diffraction signal up to a scattering angle of 13.5°.

The minimum spatial separation in the transverse direction between the two particles of the double-hit, nec-

essary to avoid the recording of the interference term, is calculated to be  $4\text{ }\mu\text{m}$ . The data employed for the reconstructions had been further rescaled in the post-processing phase, reducing the distance down to  $1\text{ }\mu\text{m}$ . Please refer to Sec. S2 of the Supplemental Material for further discussion. These quantities, and especially the  $4\text{ }\mu\text{m}$  value for the raw detector data, have to be considered an upper bound. The minimum distance can be further reduced by the limited temporal and spatial coherence of the FEL pulse, assumed to be fully coherent in those calculations.

## 2. Two-color experiment at the European XFEL

The experiment was performed at the Nano-sized Quantum Systems (NQS) endstation of the Small Quantum Systems (SQS) instrument [73–75], located on the SASE3 branch of the European XFEL [76]. The XFEL was operated at a repetition rate of 10 Hz with an electron energy of 16 GeV.

Two consecutive sets of XFEL undulators were tuned to 992 eV and 1192 eV, respectively. A magnetic chicane located after the first undulator section delayed the arrival of the electron bunch at the second undulator, introducing a time delay of 750 fs between the 992 eV pulse and the subsequent 1192 eV pulse. This enables a *pump–probe* scheme in which both X-ray pulses are generated by the XFEL [19].

The two pulses, each with a nominal duration of 20 fs, were focused to a  $5\text{ }\mu\text{m}$  spot in the interaction region [19, 75], where they intercepted isolated superfluid helium nanodroplets doped with xenon atoms. The scattered light from doped helium nanodroplets, generated by both pulses, was recorded by a pnCCD detector [26] positioned at the back of the interaction region. The geometry allows capturing scattering signals up to an angle of  $6.4^\circ$  at the edge of the detector.

In this special XFEL operation mode, the intensity at the focus is significantly reduced because each pulse is produced and amplified by only half of the available undulator sections, which are tuned to different wavelengths [19]. Consequently, the energy per pulse is reduced to  $0.7\text{ mJ}$ , compared to more than  $4\text{ mJ}$  in standard single-color operation. Furthermore, the physical separation between the undulator sections means the two collinear pulses are focused at slightly different downstream positions. As a result, the optimal focus for two-color operation lies between these two positions, with an estimated effective focal spot size of  $14\text{ }\mu\text{m}$  [35].

The combined effect of reduced pulse energy and increased focal spot size yields a nominal maximum intensity of approximately  $10^{16}\text{ W/cm}^2$ , about two orders of magnitude lower than that achieved in single-color mode.

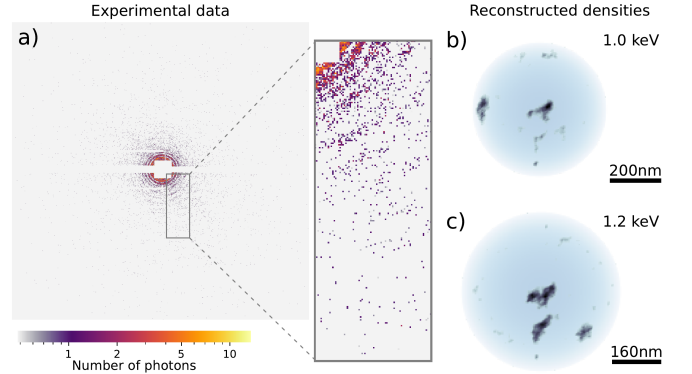


FIG. 7. Reconstruction of a xenon-doped helium nanodroplet from a two-color diffraction pattern. The figure presents the same data shown in Fig. 4a–c. However, in this case, the two reconstructed frames in panels b) and c) are not rescaled to match a common size bar and retain their original pixel dimensions.

## Appendix E: Retrieving the shape of helium droplets

The Droplet-CDI (DCDI) method [36] constrains the density distribution of the helium droplet during the reconstruction process, such that the *phase retrieval* task only involves reconstructing the density values of the inner xenon doping. The use of the DCDI method made it possible to analyze the two-color diffraction images with *Dichography*, as it greatly reduces the complexity of the imaging problem and makes it significantly more resilient to noise.

The applicability of the DCDI method to the two-color *pump–probe* data relies on two fundamental prerequisites: the ability to determine the droplet size *a priori*, and the structural integrity of the droplet, which must be preserved over the 750 fs time delay between the two XFEL pulses. Both of these conditions have been verified and demonstrated in Ref. [35], and the main findings are summarized below.

For a spherical particle, the scattered field can be calculated exactly and analytically using Mie theory, which provides solutions to Maxwell's equations [77]. The scattering signal can be fully computed with knowledge of the droplet size  $D$ , the radiation wavelength  $\lambda$ , the refractive index of the material  $n^{He}(\lambda)$  at the given photon energy, and the energy density of the light field.

For a diffraction signal from the same pure-helium droplet, composed of the incoherent sum of two different colors, Ref. [35] shows that it is possible to retrieve the size of the droplet and the intensity of the two pulses by fitting the recorded radial intensity profile as the incoherent sum of two Mie-calculated intensities, one for each color. In this procedure, the droplet size  $D$  is assumed constant between the two scattering events, while the wavelengths of the two pulses,  $\lambda^A = 1.25\text{ nm}$  and  $\lambda^B = 1.04\text{ nm}$ , as well as the corresponding refractive indices for helium,  $n^{He}(\lambda^A)$  and  $n^{He}(\lambda^B)$  [49], are known

*a priori*.

Furthermore, the comparison between the fitted scattering profiles and the experimental data reveals full compatibility of the recorded signal with that produced by a hard sphere, even for the signal produced by the late pulse arriving on the sample after 750 fs. This compatibility is experimentally verified up to a spatial resolution of 19 nm, corresponding to the momentum transfer for the 1192 eV photon energy at a 1.5° scattering angle. This angle has been identified as the maximum at which the signal-to-noise ratio in the recorded data is sufficiently high to provide useful information, as discussed in Ref. [35].

The observation about the integrity of helium droplets can be supported by theoretical considerations. The maximum number of electrons  $n_{e,out}$  that can leave the droplet due to the interaction with the first pulse can be calculated via  $n_{e,out} = (h\nu - I_p)4\pi\epsilon_0 Re^{-2}$  [78]. For a droplet with radius  $R = 350$  nm and photon energy 992 eV, this corresponds to  $n_{e,out} = 2.38 \times 10^5$  charges. This value fixes the maximum kinetic energy of a helium ion leaving the droplet and sets an upper bound to the maximum distance reached by the ion in 750 fs, estimated as 18.6 nm (see Sec. S5 of the Supplemental Material [34]). This upper bound is already below the 19 nm resolution limit of the experiment.

The physical system is thus compatible with a compact spherical helium nanodroplet for both the *pump* and the *probe* pulses, as supported by both experimental observations and theoretical considerations. Furthermore, it is possible to extract the droplet size in a precise and consistent way by fitting Mie solutions to Maxwell's equations for a signal produced by two different photon energies. For a thorough investigation of the physical system and the fitting procedure, please refer to Ref. [35]. This provides the a-priori information necessary for the use of the DCDI method during the imaging process with *Dichography*.

As discussed in Sec. A 3, the iterative approach to *Dichography* retains the real-space operations of the conventional iterative phase retrieval algorithms for CDI. The

DCDI method is, in practice, an additional real-space constraint and can be directly implemented in the algorithm workflow (see Fig. 5). The only required additional step is to properly adapt the droplet size of the density profile to the corresponding spatial resolution for the two frames,  $\rho^A$  and  $\rho^B$ .

In fact, the spatial extension of a single pixel in the reconstruction corresponds to the *half-period* resolution [7]. In the *small-angle* approximation [6], the spatial extension of a single reconstruction pixel  $\Delta$  can be calculated as:

$$\Delta = \frac{\lambda}{2 \sin(\theta_{\max})} \quad (E1)$$

where  $\lambda$  is the radiation wavelength and  $\theta_{\max}$  is the angle measured from the center of the detector to its side edge. For a two-color reconstruction with *Dichography*, the two frames correspond to two views of the same sample obtained with different colors. As such, the corresponding pixel size  $\Delta$  differs. In particular, the values for the 1.0 keV ( $\lambda = 1.25$  nm) pulse and the 1.2 keV ( $\lambda = 1.04$  nm) pulse can be calculated via Eq. (E1) as  $\Delta^{1.0\text{keV}} = 5.57$  nm and  $\Delta^{1.2\text{keV}} = 4.64$  nm.

As a consequence, when reconstructing a sample of size  $D$ , the 1.0 keV reconstruction will have an extent of  $D/\Delta^{1.0\text{keV}}$  pixels, while the 1.2 keV reconstruction will extend over  $D/\Delta^{1.2\text{keV}}$  pixels. To better highlight this aspect, we report in Fig. 7 the same two-color reconstruction shown in Fig. 4a-c, where the two retrieved frames are not scaled to match the spatial extension; i.e., they are cropped from the reconstructed matrices  $\rho^A$  and  $\rho^B$  with the same pixel dimensions. On the one hand, this representation helps the reader visualize the lower resolution of the 1.0 keV pulse. On the other hand, it highlights that the appearance of two similar structures in the two frames cannot derive from a *ghosting* effect. In fact, the arising of a reconstruction feature in the wrong frame wouldn't match the proper spatial resolution, since the two structures differ in pixel extent.

---

[1] Z. Guo, T. Driver, S. Beauvarlet, D. Cesar, J. Duris, P. L. Franz, O. Alexander, D. Bohler, C. Bostedt, V. Averbukh, *et al.*, Experimental demonstration of attosecond pump–probe spectroscopy with an x-ray free-electron laser, *Nature Photonics* **18**, 691 (2024).

[2] P. Franz, S. Li, T. Driver, R. R. Robles, D. Cesar, E. Isele, Z. Guo, J. Wang, J. P. Duris, K. Larsen, *et al.*, Terawatt-scale attosecond x-ray pulses from a cascaded superradiant free-electron laser, *Nature Photonics* **18**, 698 (2024).

[3] J. Yan, W. Qin, Y. Chen, W. Decking, P. Dijkstal, M. Guetg, I. Inoue, N. Kujala, S. Liu, T. Long, *et al.*, Terawatt-attosecond hard x-ray free-electron laser at high repetition rate, *Nature Photonics* **18**, 1293 (2024).

[4] P. K. Maroju, C. Grazioli, M. Di Fraia, M. Moioli, D. Ertel, H. Ahmadi, O. Plekan, P. Finetti, E. Allaria, L. Giannessi, *et al.*, Complex attosecond waveform synthesis at fel fermi, *Applied Sciences* **11**, 9791 (2021).

[5] J. Duris, S. Li, T. Driver, E. G. Champenois, J. P. MacArthur, A. A. Lutman, Z. Zhang, P. Rosenberger, J. W. Aldrich, R. Coffee, *et al.*, Tunable isolated attosecond x-ray pulses with gigawatt peak power from a free-electron laser, *Nature Photonics* **14**, 30 (2020).

[6] R. A. Kirian and H. N. Chapman, Imaging of objects by coherent diffraction of x-ray free-electron laser pulses, in *Synchrotron Light Sources and Free-Electron Lasers* (Springer International Publishing, 2016) pp. 1135–1195.

[7] A. Colombo and D. Rupp, Imaging clusters and their dynamics with single-shot coherent diffraction (2023).

[8] H. N. Chapman, A. Barty, M. J. Bogan, S. Boutet, M. Frank, S. P. Hau-Riege, S. Marchesini, B. W. Woods,

S. Bajt, W. H. Benner, *et al.*, Femtosecond diffractive imaging with a soft-x-ray free-electron laser, *Nature Physics* **2**, 839 (2006).

[9] T. Kimura, Y. Joti, A. Shibuya, C. Song, S. Kim, K. Tono, M. Yabashi, M. Tamakoshi, T. Moriya, T. Oshima, *et al.*, Imaging live cell in micro-liquid enclosure by x-ray laser diffraction, *Nat. Commun.* **5**, 3052 (2014).

[10] M. M. Seibert, T. Ekeberg, F. R. N. C. Maia, M. Svenda, J. Andreasson, O. Jönsson, D. Odić, B. Iwan, A. Rocker, D. Westphal, M. Hantke, D. P. DePonte, A. Barty, J. Schulz, L. Gumprecht, N. Coppola, A. Aquila, M. Liang, T. A. White, A. Martin, C. Caleman, S. Stern, C. Abergel, V. Seltzer, J.-M. Claverie, C. Bostedt, J. D. Bozek, S. Boutet, A. A. Miahnahri, M. Messerschmidt, J. Krzywinski, G. Williams, K. O. Hodgson, M. J. Bogan, C. Y. Hampton, R. G. Sierra, D. Starodub, I. Andersson, S. Bajt, M. Barthelmess, J. C. H. Spence, P. Fromme, U. Weierstall, R. Kirian, M. Hunter, R. B. Doak, S. Marchesini, S. P. Hau-Riege, M. Frank, R. L. Shoeman, L. Lomb, S. W. Epp, R. Hartmann, D. Rolles, A. Rudenko, C. Schmidt, L. Foucar, N. Kimmel, P. Holl, B. Rudek, B. Erk, A. Hömke, C. Reich, D. Pietschner, G. Weidenspointner, L. Strüder, G. Hauser, H. Gorke, J. Ullrich, I. Schlichting, S. Herrmann, G. Schaller, F. Schopper, H. Soltau, K.-U. Kühnel, R. Andritschke, C.-D. Schröter, F. Krasniqi, M. Bott, S. Schorb, D. Rupp, M. Adolph, T. Gorkhover, H. Hirsemann, G. Potdevin, H. Graafsma, B. Nilsson, H. N. Chapman, and J. Hajdu, Single mimivirus particles intercepted and imaged with an X-ray laser, *Nature* **470**, 78 (2011).

[11] T. Ekeberg, D. Assalaanova, J. Bielecki, R. Boll, B. J. Daurer, L. A. Eichacker, L. E. Franken, D. E. Galli, L. Gelisio, L. Gumprecht, *et al.*, Observation of a single protein by ultrafast x-ray diffraction, *Light: Science & Applications* **13**, 15 (2024).

[12] A. Colombo, S. Dold, P. Kolb, N. Bernhardt, P. Behrens, J. Correa, S. Düsterer, B. Erk, L. Hecht, A. Heilrath, R. Irsig, N. Iwe, J. Jordan, B. Kruse, B. Langbehn, B. Manschwetus, F. Martinez, K.-H. Meiwe-Broer, K. Oldenburg, C. Passow, C. Peltz, M. Sauppe, F. Seel, R. M. P. Tanyag, R. Treusch, A. Ulmer, S. Walz, T. Fennel, I. Barke, T. Möller, B. von Issendorff, and D. Rupp, Three-dimensional femtosecond snapshots of isolated faceted nanostructures, *Sci. Adv.* **9**, eade5839 (2023).

[13] B. Langbehn, K. Sander, Y. Ovcharenko, C. Peltz, A. Clark, M. Coreno, R. Cucini, M. Drabbels, P. Finetti, M. Di Fraia, L. Giannessi, C. Grazioli, D. Iablonskyi, A. C. LaForge, T. Nishiyama, V. Oliver Álvarez de Lara, P. Piseri, O. Plekan, K. Ueda, J. Zimmermann, K. C. Prince, F. Stienkemeier, C. Callegari, T. Fennel, D. Rupp, and T. Möller, Three-Dimensional Shapes of Spinning Helium Nanodroplets, *Phys. Rev. Lett.* **121**, 255301 (2018).

[14] T. Gorkhover, S. Schorb, R. N. Coffee, M. Adolph, L. Foucar, D. Rupp, A. Aquila, J. D. Bozek, S. W. Epp, B. Erk, L. Gumprecht, L. Holmegaard, A. Hartmann, R. Hartmann, G. Hauser, P. Holl, A. Hömke, P. Johnsson, N. Kimmel, K. U. Kühnel, M. Messerschmidt, C. Reich, A. Rouzée, B. Rudek, C. Schmidt, J. Schulz, H. Soltau, S. Stern, G. Weidenspointner, B. White, J. Küpper, L. Strüder, I. Schlichting, J. Ullrich, D. Rolles, A. Rudenko, T. Möller, and C. Bostedt, Femtosecond and nanometre visualization of structural dynamics in superheated nanoparticles, *Nature Photonics* **10**, 93 (2016).

[15] L. Flückiger, D. Rupp, M. Adolph, T. Gorkhover, M. Krikunova, M. Müller, T. Oelze, Y. Ovcharenko, M. Sauppe, S. Schorb, C. Bostedt, S. Düsterer, M. Harmand, H. Redlin, R. Treusch, and T. Möller, Time-resolved x-ray imaging of a laser-induced nanoplasma and its neutral residuals, *New J. Phys.* **18**, 043017 (2016).

[16] B. Langbehn, Y. Ovcharenko, A. Clark, M. Coreno, R. Cucini, A. Demidovich, M. Drabbels, P. Finetti, M. D. Fraia, L. Giannessi, C. Grazioli, D. Iablonskyi, A. C. LaForge, T. Nishiyama, V. O. Á. de Lara, C. Peltz, P. Piseri, O. Plekan, K. Sander, K. Ueda, T. Fennel, K. C. Prince, F. Stienkemeier, C. Callegari, T. Möller, and D. Rupp, Diffraction imaging of light induced dynamics in xenon-doped helium nanodroplets, *New J. Phys.* **24**, 113043 (2022).

[17] C. Bacellar, A. S. Chatterley, F. Lackner, C. D. Pemmaraju, R. M. P. Tanyag, D. Verma, C. Bernardo, S. M. O. O'Connell, M. Bucher, K. R. Ferguson, T. Gorkhover, R. N. Coffee, G. Coslovich, D. Ray, T. Osipov, D. M. Neumark, C. Bostedt, A. F. Vilesov, and O. Gessner, Anisotropic Surface Broadening and Core Depletion during the Evolution of a Strong-Field Induced Nanoplasma, *Phys. Rev. Lett.* **129**, 073201 (2022).

[18] S. Dold, T. Reichenbach, A. Colombo, J. Jordan, I. Barke, P. Behrens, N. Bernhardt, J. Correa, S. Düsterer, B. Erk, T. Fennel, L. Hecht, A. Heilrath, R. Irsig, N. Iwe, P. Kolb, B. Kruse, B. Langbehn, B. Manschwetus, P. Marienhagen, F. Martinez, K.-H. Meiwe-Broer, K. Oldenburg, C. Passow, C. Peltz, M. Sauppe, F. Seel, R. M. P. Tanyag, R. Treusch, A. Ulmer, S. Walz, M. Moseler, T. Möller, D. Rupp, and B. von Issendorff, Melting, bubblelike expansion, and explosion of superheated plasmonic nanoparticles, *Phys. Rev. Lett.* **134**, 136101 (2025).

[19] S. Serkez, W. Decking, L. Froehlich, N. Gerasimova, J. Grünert, M. Guetg, M. Huttula, S. Karabekyan, A. Koch, V. Kocharyan, *et al.*, Opportunities for two-color experiments in the soft x-ray regime at the european xfel, *Applied Sciences* **10**, 2728 (2020).

[20] A. Lutman, R. Coffee, Y. Ding, Z. Huang, J. Krzywinski, T. Maxwell, M. Messerschmidt, and H.-D. Nuhn, Experimental demonstration of femtosecond two-color x-ray free-electron lasers, *Physical Review Letters* **110**, 134801 (2013).

[21] A. Marinelli, D. Ratner, A. Lutman, J. Turner, J. Welch, F.-J. Decker, H. Loos, C. Behrens, S. Gilevich, A. Miahnahri, S. Vetter, T. Maxwell, Y. Ding, R. Coffee, S. Wakatsuki, and Z. Huang, High-intensity double-pulse X-ray free-electron laser, *Nature Communications* **6**, 6369 (2015).

[22] E. Allaria, D. Castronovo, P. Cinquegrana, P. Craievich, M. Dal Forno, M. Danailov, G. D'Auria, A. Demidovich, G. De Ninno, S. Di Mitri, *et al.*, Two-stage seeded soft-x-ray free-electron laser, *Nature Photonics* **7**, 913 (2013).

[23] T. Hara, Y. Inubushi, T. Katayama, T. Sato, H. Tanaka, T. Tanaka, T. Togashi, K. Togawa, K. Tono, M. Yabashi, *et al.*, Two-colour hard x-ray free-electron laser with wide tunability, *Nature Communications* **4**, 2919 (2013).

[24] E. Prat, P. Dijkstal, E. Ferrari, R. Ganter, P. Juranić, A. Malyzhenkov, S. Reiche, T. Schietinger, G. Wang, A. A. Haddad, *et al.*, Widely tunable two-color x-ray free-electron laser pulses, *Physical Review Research* **4**,

L022025 (2022).

[25] L. Strüder, S. Epp, D. Rolles, R. Hartmann, P. Holl, G. Lutz, H. Soltau, R. Eckart, C. Reich, K. Heinzinger, C. Thamm, A. Rudenko, F. Krasniqi, K.-U. Kühnel, C. Bauer, C.-D. Schröter, R. Moshammer, S. Techert, D. Miessner, M. Porro, O. Hälker, N. Meidinger, N. Kimmel, R. Andritschke, F. Schopper, G. Weidenspointner, A. Ziegler, D. Pietschner, S. Herrmann, U. Pietsch, A. Walenta, W. Leitenberger, C. Bostedt, T. Möller, D. Rupp, M. Adolph, H. Graafsma, H. Hirsemann, K. Gärtner, R. Richter, L. Foucar, R. L. Shoeman, I. Schlichting, and J. Ullrich, Large-format, high-speed, X-ray pnCCDs combined with electron and ion imaging spectrometers in a multipurpose chamber for experiments at 4th generation light sources, Nuclear Instruments and Methods in Physics Research Section A: Accelerators, Spectrometers, Detectors and Associated Equipment **614**, 483 (2010).

[26] M. Kuster, K. Ahmed, K.-E. Ballak, C. Danilevski, M. Ekmedžić, B. Fernandes, P. Gessler, R. Hartmann, S. Hauf, P. Holl, M. Meyer, J. Montaño, A. Münnich, Y. Ovcharenko, N. Rennhack, T. Rüter, D. Rupp, D. Schlosser, K. Setoodehnia, R. Schmitt, L. Strüder, R. M. P. Tanyag, A. Ulmer, and H. Yousef, The 1-megapixel pnccd detector for the small quantum systems instrument at the european xfel: system and operation aspects, J. Synchrotron Radiat. **28**, 576 (2021).

[27] V. Hinger, A. al Haddad, R. Barten, A. Bergamaschi, M. Brückner, M. Carulla, S. Chirietti-Alvarez, R. Di-napoli, S. Ebner, E. Fröjd, *et al.*, Advancing the jungfrau detector toward low-energy x-ray applications, Journal of Instrumentation **17** (09), C09027.

[28] S. Marchesini, H. He, H. N. Chapman, S. P. Hau-Riege, A. Noy, M. R. Howells, U. Weierstall, and J. C. H. Spence, X-ray image reconstruction from a diffraction pattern alone, Phys. Rev. B **68**, 140101(R) (2003).

[29] K. R. Ferguson, M. Bucher, T. Gorkhov, S. Boutet, H. Fukuzawa, J. E. Koglin, Y. Kumagai, A. Lutman, A. Marinelli, M. Messerschmidt, K. Nagaya, J. Turner, K. Ueda, G. J. Williams, P. H. Bucksbaum, and C. Bostedt, Transient lattice contraction in the solid-to-plasma transition, Science Advances **2**, e1500837 (2016).

[30] L. Hecht, *Zweifarben-Streubildaufnahme von Helium-Nanotropfchen: Planung, Durchführung und erste Ergebnisse*, Master's thesis, Technische Universität Berlin, Berlin (2018).

[31] M. Sauppe, T. Bischoff, C. Bomme, C. Bostedt, A. Colombo, B. Erk, T. Feigl, L. Flückiger, T. Gorkhov, A. Heilrath, K. Kolatzki, Y. Kumagai, B. Langbehn, J. P. Möller, C. Passow, D. Ramm, D. Rolles, D. Rompotis, J. Schäfer-Zimmermann, B. Senftleben, R. Treusch, A. Ulmer, J. Zimbalski, T. Möller, and D. Rupp, Double diffraction imaging of x-ray induced structural dynamics in single free nanoparticles, New Journal of Physics **26**, 073019 (2024).

[32] S. Marchesini, Invited article: A unified evaluation of iterative projection algorithms for phase retrieval, Rev. Sci. Instrum. **78**, 011301 (2007).

[33] F. Nolting, C. Bostedt, T. Schietinger, and H. Braun, The swiss light source and swissfel at the paul scherrer institute, The European Physical Journal Plus **138**, 126 (2023).

[34] See Supplemental Material at [URL\\_will\\_be\\_provided\\_by\\_the\\_publisher](URL_will_be_provided_by_the_publisher).

[35] L. Hecht, Y. Ovcharenko, A. Ø. Lægdsmand, B. Bas-  
tian, T. M. Baumann, A. Colombo, S. De, A. D. Fanis, S. Dold, T. Fennel, R. Hartmann, K. Kolatzki, S. Krishnan, B. Kruse, A. C. Laforge, B. Langbehn, S. Mandal, T. Mazza, C. Medina, C. Peltz, T. Pfeifer, B. Senftleben, K. Sishodia, F. Stienkemeier, R. M. P. Tanyag, P. Tümmeler, S. Usenko, A. Heidenreich, M. Meyer, D. Rupp, and M. Mudrich, Two-color x-ray coherent diffraction imaging of helium nanodroplets (2025), arXiv:2508.19991.

[36] R. M. P. Tanyag, C. Bernando, C. F. Jones, C. Bacelar, K. R. Ferguson, D. Anielski, R. Boll, S. Carron, J. P. Cryan, L. Englert, *et al.*, Communication: X-ray coherent diffractive imaging by immersion in nanodroplets, Structural Dynamics **2** (2015).

[37] O. Gessner and A. F. Vilesov, Imaging quantum vortices in superfluid helium droplets, Annual review of physical chemistry **70**, 173 (2019).

[38] A. Ulmer, A. Heilrath, B. Senftleben, S. M. O'Connell-Lopez, B. Kruse, L. Seiffert, K. Kolatzki, B. Langbehn, A. Hoffmann, T. M. Baumann, *et al.*, Generation of large vortex-free superfluid helium nanodroplets, Physical review letters **131**, 076002 (2023).

[39] R. M. P. Tanyag, C. F. Jones, C. Bernando, S. M. O. O'Connell, D. Verma, and A. F. Vilesov, CHAPTER 8. Experiments with Large Superfluid Helium Nanodroplets, in *Theoretical and Computational Chemistry Series*, edited by O. Dulieu and A. Osterwalder (Royal Society of Chemistry, Cambridge, 2017) pp. 389–443.

[40] A. Colombo, M. Sauppe, A. A. Haddad, K. Ayyer, M. Babayan, R. Boll, R. Dagar, S. Dold, T. Fennel, L. Hecht, G. Knopp, K. Kolatzki, B. Langbehn, F. R. N. C. Maia, A. Mall, P. Mazumder, T. Mazza, Y. Ovcharenko, I. C. Polat, D. Raiser, J. C. Schäfer-Zimmermann, K. Schnorr, M. L. Schubert, A. Sehati, J. A. Sellberg, B. Senftleben, Z. Shen, Z. Sun, P. H. W. Svensson, P. Tümmeler, S. Usenko, C. F. Ussling, O. Veteläinen, S. Wächter, N. Walsh, A. V. Weitnauer, T. You, M. Zuod, M. Meyer, C. Bostedt, D. E. Galli, M. Patanen, and D. Rupp, SPRING, an effective and reliable framework for image reconstruction in single-particle Coherent Diffraction Imaging, npj Computational Materials **11**, 265 (2025).

[41] E. Prat, Z. Geng, C. Kittel, A. Malyzhenkov, F. Marcellini, S. Reiche, T. Schietinger, and P. Craievich, Attosecond time-resolved measurements of electron and photon beams with a variable polarization x-band radiofrequency deflector at an x-ray free-electron laser, Advanced Photonics **7**, 026002 (2025).

[42] S. Kuschel, P. J. Ho, A. Al Haddad, F. F. Zimmermann, L. Flueckiger, M. R. Ware, J. Duris, J. P. MacArthur, A. Lutman, M.-F. Lin, X. Li, K. Nakahara, J. W. Aldrich, P. Walter, L. Young, C. Bostedt, A. Marinelli, and T. Gorkhov, Non-linear enhancement of ultrafast X-ray diffraction through transient resonances, Nature Communications **16**, 10.1038/s41467-025-56046-y (2025).

[43] A. Ulmer, P. J. Ho, B. Langbehn, S. Kuschel, L. Hecht, R. Obaid, S. Dold, T. Driver, J. Duris, M.-F. Lin, D. Cesar, P. Franz, Z. Guo, P. A. Hart, A. Kamalov, K. A. Larsen, X. Li, M. Meyer, K. Nakahara, R. G. Radloff, R. Robles, L. Rönnebeck, N. Sudar, A. M. Summers, L. Young, P. Walter, J. Cryan, C. Bostedt, D. Rupp, A. Marinelli, and T. Gorkhov, Nonlinear reversal of photo-excitation on the attosecond time

scale improves ultrafast x-ray diffraction images, arXiv 10.48550/arXiv.2506.19394 (2025).

[44] J. C. Schäfer-Zimmermann, T. von Scheven, K. Koltzki, B. Kruse, B. Langbehn, T. Möller, N. Monserud, M. Sauppe, B. Schütte, B. Senftleben, R. M. P. Tanyag, A. Ulmer, T. Fennel, M. J. J. Vrakking, A. Rouzée, and D. Rupp, Laser-induced transient opacity in helium nanodroplets probed by single-shot coherent diffraction (2025), arXiv:2508.19936.

[45] C. Vicario, S. Bettoni, A. Lutman, A. Dax, M. Huppert, and A. Trisorio, Two-color x-ray free-electron laser by photocathode laser emittance spoiler, *Physical Review Accelerators and Beams* **24**, 060703 (2021).

[46] G. Marr and J. West, Absolute photoionization cross-section tables for helium, neon, argon, and krypton in the vuv spectral regions, *Atomic Data and Nuclear Data Tables* **18**, 497 (1976).

[47] E. Allaria, L. Badano, S. Bassanese, F. Capotondi, D. Castronovo, P. Cinquegrana, M. B. Danailov, G. D'Auria, A. Demidovich, R. De Monte, G. De Ninno, S. Di Mitri, B. Diviacco, W. M. Fawley, M. Ferianis, E. Ferrari, G. Gaio, D. Gauthier, L. Giannessi, F. Iazzourene, G. Kurdi, N. Mahne, I. Nikolov, F. Parmigiani, G. Penco, L. Raimondi, P. Rebernik, F. Rossi, E. Roussel, C. Scafuri, C. Serpico, P. Sigalotti, C. Spezzani, M. Svandrlík, C. Svetina, M. Trovó, M. Veronese, D. Zangrandino, and M. Zangrandino, The FERMI free-electron lasers, *Journal of Synchrotron Radiation* **22**, 485 (2015).

[48] J. Rossbach, J. R. Schneider, and W. Wurth, 10 years of pioneering X-ray science at the Free-Electron Laser FLASH at DESY, *Physics Reports* **808**, 1 (2019).

[49] B. L. Henke, E. M. Gullikson, and J. C. Davis, X-ray interactions: photoabsorption, scattering, transmission, and reflection at  $e=50\text{-}30,000$  ev,  $z=1\text{-}92$ , *Atomic data and nuclear data tables* **54**, 181 (1993).

[50] D. Rupp, L. Flückiger, M. Adolph, A. Colombo, T. Gorkhov, M. Harmand, M. Krikunova, J. P. Müller, T. Oelze, Y. Ovcharenko, *et al.*, Imaging plasma formation in isolated nanoparticles with ultrafast resonant scattering, *Structural Dynamics* **7**, 034303 (2020).

[51] A. A. Lutman, J. P. MacArthur, M. Ilchen, A. O. Lindahl, J. Buck, R. N. Coffee, G. L. Dakovski, L. Dammann, Y. Ding, H. A. Dürr, *et al.*, Polarization control in an x-ray free-electron laser, *Nature photonics* **10**, 468 (2016).

[52] C. Kittel, A. Sarracini, S. Augustin, N. Yang, A. Al Haddad, E. Ferrari, G. Knopp, J. Knurr, A. S. Morillo-Candas, I. Swiderska, *et al.*, Demonstration of full polarization control of soft x-ray pulses with apple x undulators at swissfel using recoil ion momentum spectroscopy, *Synchrotron Radiation* **31** (2024).

[53] E. Allaria, B. Diviacco, C. Callegari, P. Finetti, B. Mahieu, J. Viefhaus, M. Zangrandino, G. De Ninno, G. Lambert, E. Ferrari, *et al.*, Control of the polarization of a vacuum-ultraviolet, high-gain, free-electron laser, *Physical Review X* **4**, 041040 (2014).

[54] J. Yan, H. Hao, S. Huang, J. Li, V. N. Litvinenko, P. Liu, S. F. Mikhailov, V. G. Popov, G. Swift, N. A. Vinokurov, *et al.*, Polarization control of a free-electron laser oscillator using helical undulators of opposite helicities, *Physical Review Accelerators and Beams* **23**, 060702 (2020).

[55] S. Marotzke, D. Gupta, R.-P. Wang, M. Pavelka, S. Dziarzhytski, C. von Korff Schmising, S. Jana, N. Thielemann-Kühn, T. Amrhein, M. Weinelt, *et al.*, First experiments with ultrashort, circularly polarized soft x-ray pulses at flash2, *Structural Dynamics* **12** (2025).

[56] J. Stöhr, X-ray magnetic circular dichroism spectroscopy of transition metal thin films, *Journal of Electron Spectroscopy and Related Phenomena* **75**, 253 (1995).

[57] R. Cireasa, A. Boguslavskiy, B. Pons, M. Wong, D. Descamps, S. Petit, H. Ruf, N. Thiré, A. Ferré, J. Suarez, *et al.*, Probing molecular chirality on a sub-femtosecond timescale, *Nature Physics* **11**, 654 (2015).

[58] S. B. Wilkins, P. D. Spencer, P. D. Hatton, S. P. Collins, M. D. Roper, D. Prabhakaran, and A. T. Boothroyd, Direct observation of orbital ordering in  $\text{La}_{0.5}\text{Sr}_{1.5}\text{MnO}_4$  using soft x-ray diffraction, *Phys. Rev. Lett.* **91**, 167205 (2003).

[59] J. R. Fienup, Phase retrieval algorithms: a comparison, *Appl. Opt.* **21**, 2758 (1982).

[60] B. Abbey, L. W. Whitehead, H. M. Quiney, D. J. Vine, G. A. Cadenazzi, C. A. Henderson, K. A. Nugent, E. Balaur, C. T. Putkunz, A. G. Peele, *et al.*, Lensless imaging using broadband x-ray sources, *Nature Photonics* **5**, 420 (2011).

[61] J. Huijts, S. Fernandez, D. Gauthier, M. Kholodtsova, A. Maghraoui, K. Medjoubi, A. Somogyi, W. Boutu, and H. Merdji, Broadband coherent diffractive imaging, *Nature Photonics* **14**, 618 (2020).

[62] C. Chen, H. Gu, and S. Liu, Ultra-broadband diffractive imaging with unknown probe spectrum, *Light: Science & Applications* **13**, 213 (2024).

[63] D. Rupp, N. Monserud, B. Langbehn, M. Sauppe, J. Zimmermann, Y. Ovcharenko, T. Möller, F. Frassetto, L. Polletto, A. Trabattoni, *et al.*, Coherent diffractive imaging of single helium nanodroplets with a high harmonic generation source, *Nature communications* **8**, 493 (2017).

[64] J. Miao, D. Sayre, and H. N. Chapman, Phase retrieval from the magnitude of the fourier transforms of nonperiodic objects, *J. Opt. Soc. Am. A* **15**, 1662 (1998).

[65] V. Favre-Nicolin, F. Mastropietro, J. Eymery, D. Camacho, Y. Niquet, B. Borg, M. Messing, L.-E. Wernersson, R. Algra, E. Bakkers, *et al.*, Analysis of strain and stacking faults in single nanowires using bragg coherent diffraction imaging, *New Journal of Physics* **12**, 035013 (2010).

[66] M. Guizar-Sicairos and P. Thibault, Ptychography: A solution to the phase problem, *Physics Today* **74**, 42 (2021).

[67] A. Colombo, D. E. Galli, L. De Caro, F. Scattarella, and E. Carlino, Facing the phase problem in coherent diffractive imaging via memetic algorithms, *Sci. Rep.* **7**, 42236 (2017).

[68] Z. Sun, A. Al Haddad, S. Augustin, G. Knopp, J. Knurr, K. Schnorr, and C. Bostedt, Ultrafast single-particle imaging with intense x-ray pulses, *Chimia* **76**, 529 (2022).

[69] PSI, Swissfel maloja experimental station (Aug 2025), <https://www.psi.ch/en/swissfel/maloja>.

[70] J. Bielecki, M. F. Hantke, B. J. Daurer, H. K. Reddy, D. Hasse, D. S. Larsson, L. H. Gunn, M. Svenda, A. Munke, J. A. Sellberg, *et al.*, Electrospray sample injection for single-particle imaging with x-ray lasers, *Science Advances* **5**, eaav8801 (2019).

[71] M. F. Hantke, J. Bielecki, O. Kulyk, D. Westphal, D. S. Larsson, M. Svenda, H. K. Reddy, R. A. Kirian, J. Andreasson, J. Hajdu, *et al.*, Rayleigh-scattering microscopy for tracking and sizing nanoparticles in focused aerosol beams, *IUCrJ* **5**, 673 (2018).

[72] A. Mozzanica, M. Andrä, R. Barten, A. Bergamaschi, S. Chirietti, M. Brückner, R. Dinapoli, E. Fröjdahl, D. Greiffenberg, F. Leonarski, *et al.*, The jungfrau detector for applications at synchrotron light sources and xfel, *Synchrotron Radiation News* **31**, 16 (2018).

[73] SQS, Small Quantum Systems Instrument (Aug 2025), [https://www.xfel.eu/facility/instruments/sqs/index\\_eng.html](https://www.xfel.eu/facility/instruments/sqs/index_eng.html).

[74] T. Tschentscher, C. Bressler, J. Grünert, A. Madsen, A. P. Mancuso, M. Meyer, A. Scherz, H. Sinn, and U. Zastrau, Photon beam transport and scientific instruments at the european xfel, *Applied Sciences* **7**, 592 (2017).

[75] T. Mazza, T. M. Baumann, R. Boll, A. De Fainis, P. Grychtol, M. Ilchen, J. Montaño, V. Music, Y. Ovcharenko, N. Rennhack, D. E. Rivas, A. Rörig, P. Schmidt, S. Usenko, P. Ziolkowski, D. La Civita, M. Vannoni, H. Sinn, B. Keitel, E. Plönjes, U. F. Jastrow, A. Sorokin, K. Tiedtke, K. Mann, B. Schäfer, N. Breckwoldt, S.-K. Son, and M. Meyer, The beam transport system for the Small Quantum Systems instrument at the European XFEL: Optical layout and first commissioning results, *Journal of Synchrotron Radiation* **30**, 457 (2023).

[76] W. Decking, S. Abeghyan, P. Abramian, A. Abramsky, A. Aguirre, C. Albrecht, P. Alou, M. Altarelli, P. Altmann, K. Amyan, *et al.*, A mhz-repetition-rate hard x-ray free-electron laser driven by a superconducting linear accelerator, *Nat. Photonics* **14**, 391 (2020).

[77] G. Mie, Beiträge zur Optik trüber Medien, speziell kolloidaler Metallösungen, *Annalen der Physik* 10.1002/andp.19083300302 (1908).

[78] C. Bostedt, H. Thomas, M. Hoener, T. Möller, U. Saalmann, I. Georgescu, C. Gnodtke, and J.-M. Rost, Fast electrons from multi-electron dynamics in xenon clusters induced by inner-shell ionization, *New J. Phys.* **12**, 083004 (2010).